Neutron Scattering Studies of Spin Glass Behaviour in $LiNiO_2$

NEUTRON SCATTERING STUDIES OF SPIN GLASS BEHAVIOUR IN $LiNiO_2$

By

JAMES PATRICK IAN CLANCY, B.Sc.

A Thesis
Submitted to the School of Graduate Studies
in Partial Fulfillment of the Requirements
for the Degree
Master of Science

McMaster University

MASTER OF SCIENCE (2006)
(Physics)

McMaster University
Hamilton, Ontario

TITLE: Neutron Scattering Studies of Spin Glass Behaviour in $LiNiO_2$

AUTHOR: James Patrick Ian Clancy, B.Sc. (St. Francis Xavier University)

SUPERVISOR: Dr. B.D. Gaulin

NUMBER OF PAGES: viii, 58

Abstract

We have performed time-of-flight neutron scattering measurements on two polycrystalline samples of $LiNiO_2$ using the Disk Chopper Spectrometer at the NIST Center for Neutron Research. These measurements reveal an absence of magnetic Bragg peaks, indicating a lack of magnetic order down to 1.7K. In addition, we observe a significant narrowing in the width of the inelastic scattering at $T_g \sim 9K$, which is accompanied by a simultaneous increase in the intensity of the elastic magnetic scattering. This provides direct evidence of a spin glass transition at T_g, implying that the low temperature magnetic state of $LiNiO_2$ is composed of frozen, disordered moments. Similar time-of-flight studies performed on $NaNiO_2$, the isostructural sister compound of $LiNiO_2$, have shown the existence of a simple magnetic structure below $T_N \sim 23K$, consisting of ferromagnetic sheets of spin 1/2 moments stacked in an antiferromagnetic fashion [1]. From the distinct similarities observed between the inelastic magnetic scattering in $LiNiO_2$ and paramagnetic $NaNiO_2$, it is implied that the low $|Q|$ spin response in $LiNiO_2$ may originate from the collapse of short-lived spin wave modes below the (0,0,1/2) position, the lowest wave vector of antiferromagnetic ordering. It is suggested that inherent chemical disorder in $LiNiO_2$, caused by the substitution of Ni^{3+} and Li^{+} ions within the crystal structure, results in the frustration of inter-layer magnetic interactions, thereby preventing the development of a magnetically long range ordered state.

Acknowledgements

This project would not have been possible without numerous contributions from the many talented scientists that I have had the opportunity to work with over the past two years. First and foremost, I would like to thank my supervisor, Dr. Bruce Gaulin, who was involved in every aspect of this work, and whose expert advice has guided this project from start to finish. I look forward to continuing my work with Bruce in the future. I would also like to thank the other members of my supervisory committee, Dr. Graeme Luke and Dr. An-Chang Shi, whom I will almost undoubtedly be forcing to read this thesis upon unfairly short notice.

I would like to acknowledge the support of the National Institute of Standards and Technology (NIST) in providing the neutron research facilities used in this work. In particular, it is important to recognize the contributions of John Copley and Yiming Qiu, the instrument scientists on the Disk Chopper Spectrometer, whose expertise proved invaluable throughout the experiment. Neutron scattering measurements were also performed with the assistance of Sarah Dunsiger and Sara Haravifard.

Samples for the $LiNiO_2$ experiment were graciously provided by Moli Energy (1990) Limited and the National Research Council of Canada. I am also grateful for the previous sample characterization measurements carried out on these samples by J.N. Reimers, J.R. Dahn, J.E. Greedan, C.V. Stager, G. Liu, I. Davidson, and U. von Sacken in 1993 and by J. van Duijn, J.M.S. Park, and S.-H. Lee in 2001. The x-ray structure refinements performed by these groups, in particular, were extremely helpful during the interpretation of our experimental results.

$NaNiO_2$ neutron scattering data, which has been reanalysed for the purpose of this work, was originally collected in 2003 by Mike Lewis, Bruce Gaulin, Yiming

Qiu and John Copley. The $NaNiO_2$ samples used in this experiment were prepared at McMaster University by Hanna Dabkowska and Israel Crooks.

Thanks to all of my friends and colleagues in the x-ray and neutron scattering group at McMaster: John-Paul Castellan, Jacob Ruff, Yang Zhao, Sara Haravifard, Sarah Dunsiger and Kirrily Rule. It has been a pleasure to work with you over the last two years.

I would like to acknowledge the generous financial support provided by NSERC of Canada, in addition to the more modest (but far more entertaining) financial contributions of the Condensed Matter Poker Society.

Finally, I would like to offer a special thanks to my parents and my beautiful girlfriend Shauna for their continued patience, love and support.

Contents

List of Figures

Chapter 1

Introduction

The nature of the magnetic ground state in $LiNiO_2$ has been the subject of considerable speculation and debate for more than two decades. Over this period of time, an impressively large number of novel, and often very contradictory, magnetic ground states have been proposed for the system. $LiNiO_2$ has been described as a spin liquid [2, 3, 4, 5], a spin glass [6, 7], a 2D Ising ferromagnet [8], a 2D Heisenberg ferromagnet [9], a 2D frustrated antiferromagnet [10], a quantum disordered state [11], a collection of ferrimagnetic clusters [12, 13], and many other variations on these scenarios [14, 15, 16, 17, 18]. It is the somewhat elusive character of the ground state in $LiNiO_2$ which has largely been responsible for the continued interest in the material.

Studies of $LiNiO_2$ were originally motivated by the proposal of Hirakawa et al. [2] that the material might represent the first experimental realization of a 2-dimensional spin 1/2 triangular lattice antiferromagnet. This combination of triangular lattice geometry and antiferromagnetically-coupled spins is known to give rise to competition between the structural and magnetic constraints of the system. The resulting phenomenon, commonly referred to as geometrical frustration, is widely appreciated to be a potential source of unusual physics and exotic quantum mechanical ground states [19]. In fact, it was the 2-dimensional spin 1/2 triangular lattice antiferromagnet which first led Anderson to suggest the possible existence of the resonating valence bond (RVB) or spin liquid state [20]. While no direct evidence of an RVB state has been observed in $LiNiO_2$ to date, spin liquid remains one of the descriptions most frequently applied to the material [5].

To a large extent, widespread speculation about the nature of the magnetic ground state has been fuelled by experimental measurements which indicate an absence of either magnetic or orbital long range order down to extremely low temperatures [2, 21]. These observations are particularly intriguing in light of the fact that $NaNiO_2$, the isostructural sister compound of $LiNiO_2$, is known to undergo both orbital and magnetic ordering at temperatures of $T_{JT} \sim 480K$ and $T_N \sim 23K$ respectively [1, 22]. It remains an open question as to why there should be such profound differences in the orbital and magnetic behaviour of two materials which are so closely related in structure.

Both $LiNiO_2$ and $NaNiO_2$ are quasi-two-dimensional quantum magnets, composed of stacked triangular planes which alternate between layers of alkali metal (Li^+, Na^+) and Ni^{3+} ions. At high temperatures, the two materials are isostructural, with rhombohedral crystal structures belonging to the space group $R\bar{3}m$. At $T_{JT} \sim 480K$, as noted above, $NaNiO_2$ undergoes a cooperative Jahn-Teller phase transition which results in the formation of long range orbital order. This transition is also accompanied by a distortion of the lattice, which reduces the symmetry of the crystal structure to the monoclinic space group $C2/m$. While no equivalent global or long range orbital ordering has been observed in $LiNiO_2$, both EXAFS and neutron diffraction measurements have provided evidence of local Jahn-Teller distortions which arise at approximately 400K [21, 23]. It has been suggested that these distortions correspond

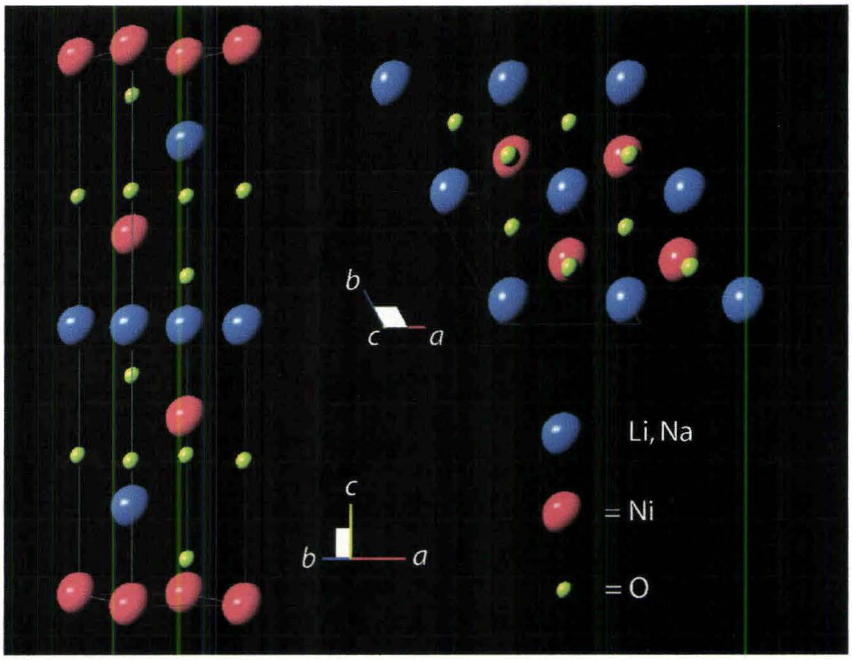

Figure 1.1: The crystal structure of $LiNiO_2$ and $NaNiO_2$.

to the formation of small domains, $\sim$ 10 nm in size, exhibiting a form of trimer ordering between the $3d_{z^2-r^2/3}$ orbitals of the Ni^{3+} ion [23].

The unit cell of $LiNiO_2$ and $NaNiO_2$ (for $T > 480K$) is illustrated in figure 1.1. Note, in particular, the triangular geometry of the Li^+/Na^+ and Ni^{3+} planes stacked along the c-direction. Each Ni^{3+} ion sits at the center of a NiO_6 octahedron, having six-fold oxygen coordination. The alkali metal ions form tetrahedrons, having an oxygen coordination number of 4. The lattice parameters of this structure are $a = b = 2.88\ \AA$ and $c = 14.20\ \AA$ for $LiNiO_2$ [6], and $a = b = 2.96\ \AA$ and $c = 15.76\ \AA$ for $NaNiO_2$ [22]. As a result, it follows that the distance between neighbouring planes of Ni^{3+} ions along the c-axis is $\sim 4.76\ \AA$ for $LiNiO_2$ and $\sim 5.25\ \AA$ for $NaNiO_2$.

The magnetism in both materials is due to the spin 1/2 moments carried by Ni^{3+} ions. In $NaNiO_2$, it is known that the intra-plane Ni-Ni interaction, J, is ferromagnetic, while the inter-plane Ni-Ni interaction, J', is antiferromagnetic. On the basis of magnetic susceptibility measurements, the values of the intra-plane and inter-plane exchange couplings have been determined to be J = 13K and J' = -1K respectively [24]. The nature of the magnetic interactions in $LiNiO_2$, meanwhile, remains the subject of considerable controversy. Over the past twenty years, magnetic susceptibility measurements have been interpreted to suggest almost any possible permutation of inter-plane and intra-plane coupling schemes [2, 6, 12, 13, 25]. From recent studies performed on high quality samples, there now appears to be some general agreement that the intra-plane Ni-Ni interaction is ferromagnetic with J $\sim$ 8K to 10K [12, 25]. The magnitude and sign of J', however, has yet to be firmly established.

While anomalies in the low temperature susceptibility of $NaNiO_2$ had long been believed to represent the onset of long range magnetic order [13, 26], the first direct evidence of a magnetically ordered ground state was provided by recent neutron scattering measurements performed by Lewis et al [1]. These measurements revealed the presence of magnetic Bragg peaks and spin waves below $T_N \sim 23$K, consistent with the development of a magnetically ordered structure. As predicted by Bongers and Enz in 1966 [26], this structure is composed of triangular layers of ferromagnetically aligned spin 1/2 moments, which are stacked in an antiferromagnetic fashion along the *c*-axis direction. Similar neutron scattering measurements on $LiNiO_2$ suggest a very different low temperature state, with no observable long range magnetic order down to temperatures of $\sim$ 1.4K [2, 27]. Evidence of diffuse scattering provided by the small angle neutron scattering measurements of Yoshikawa et al. [14], implies the existence of short-ranged ferromagnetic correlations between frozen spins, just as one might expect to find in a spin glass.

When reviewing the results of previous studies on $LiNiO_2$ and $NaNiO_2$, it is important to recognize that there are a number of significant experimental challenges which potentially hinder any investigation of these two materials. One of the principal difficulties is that neither $LiNiO_2$ or $NaNiO_2$ can be produced in single crystal form. As a result, any study of these materials must be performed on polycrystalline or powder samples, a restriction which imposes substantial limits on the nature of the physical information which can be measured. In addition, since each formula unit of $LiNiO_2$ or $NaNiO_2$ contains only a single spin 1/2 moment, the effectiveness of measurements specifically related to the magnetic properties of these materials is potentially limited by both the small size and low density of the magnetic moments.

Studies of $LiNiO_2$ are further complicated by the similar sizes of the Ni^{3+} and Li^+ ions, which inherently leads to substitution between the Ni^{3+} and Li^+ sublattices. In $NaNiO_2$, the relatively large size of the Na^+ ion, which has an ionic radius of ~ 1.15 $\mathring{A}$, makes this form of ionic mixing quite unlikely. However, since Ni^{3+} and Li^+ have almost identical ionic radii of ~ 0.7 $\mathring{A}$, a certain degree of chemical disorder due to Ni^{3+}/Li^+ substitution is believed to be inevitable in $LiNiO_2$ [13]. As a result, the compound $LiNiO_2$ is more accurately described as $Li_{1-x}Ni_{1+x}O_2$, where the parameter x refers to the fractional deficiency of Li in the material. For the majority of the samples reported in the published literature, the value of x lies between 0.4% [13] and 10% [6, 15]. Systematic studies of the $Li_{1-x}Ni_{1+x}O_2$ system for $0.004 < x < 0.36$ [6, 21, 25, 12, 13] indicate that sample stoichiometry has a profound influence on the resulting magnetic properties of the material. This would seem to suggest that it is the inherent chemical disorder of $LiNiO_2$, which is known to vary significantly from sample to sample, that holds the key to understanding why so many conflicting and apparently contradictory results have been reported for this material in the past.

It should also be noted that $LiNiO_2$ is a particularly difficult system to study with neutron scattering. This is due to the presence of Li, or more specifically ^6Li, an isotope of Li which has an exceptionally high neutron absorption cross section. Even with ^{6}Li representing only 7.5% of natural Li, the resulting absorption cross section of the element is more than 15 times greater than that of Ni, and over two orders of magnitude greater than that of Na [28]. While there are a number of ways to deal with the problems which arise from a strongly absorbing sample, as will be discussed in the following chapters, it should be relatively unsurprising that there have been few detailed neutron studies of $LiNiO_2$ in the past.

In the following chapters of this thesis, I will describe the results of a recent study of $LiNiO_2$ using time-of-flight neutron scattering techniques. Following a brief introduction to the theory of neutron scattering and the time-of-flight technique, I will discuss how the two samples used in this experiment were synthesized, characterized, and studied by neutron scattering. I will describe a number of interesting experimental results which emerged from this study, drawing frequent comparisons between our measurements on $LiNiO_2$ and those performed by Lewis et al. [1] on $NaNiO_2$. To conclude, I will attempt to explain the physical implications of our results and what they may reveal about the low temperature magnetic state of $LiNiO_2$.

Chapter 2

Experimental Details

As noted in chapter 1 during our review of previous experimental results, the magnetic properties of $LiNiO_2$ exhibit a striking dependence on sample stoichiometry and preparation conditions. Thus, before proceeding with any discussion of experimental results, it is important to examine the methods by which the samples used in this experiment were synthesized and characterized prior to study. In the following sections, I will describe the synthesis of the three samples which we have studied using time-of-flight neutron scattering ($LiNiO_2$ (X), $LiNiO_2$ (D), and $NaNiO_2$). Where appropriate, I will discuss the results of the magnetic susceptibility and x-ray diffraction measurements which have been used to characterize these samples, and I will provide a brief overview of the experimental details relevant to our time-of-flight measurements.

2.1 Sample Synthesis

In this experiment, measurements were performed on polycrystalline samples of $LiNiO_2$, referred to as (X) and (D), which were prepared using two different methods of synthesis. $LiNiO_2$ (X) was prepared by Moli Energy (1990) Limited in

Burnaby, British Columbia, while $LiNiO_2$ (D) was provided by the National Research Council (NRC) of Canada located in Ottawa, Ontario.

$LiNiO_2$ (X) was prepared from starting materials of $LiOH \bullet H_2O$ and NiO. These materials were mixed with a Li:Ni ratio of 1.1:1 in an effort to minimize the substitution of Ni and Li ions. The mixture was then subjected to three bakings at 650 C, for durations of 4.5, 12.5, and 4 hours respectively, with grindings of the sample performed between each firing. The first and second firings of the sample were performed in an atmosphere free of both moisture and CO_2, while the third firing was carried out at an absolute humidity corresponding to a dew point of -40 C.

The second sample, $LiNiO_2$ (D), was synthesized from an equal weight mixture of $LiOH \bullet H_2O$ and $NiO_2 \bullet H_2O$. As in the case of the previous sample, the proportions of these starting materials were chosen to ensure the presence of excess Li in the initial mixture. The mixture was ground and formed into pellets, which were then heated for 3 hours at 200C in an O_2 environment. This was followed by a second heating at 800 C for 35 hours, after which the resulting sample was washed with both water and ethanol, and then dried for several hours at 100 C.

As noted by Reimers et al. [6], the firing temperature of $LiNiO_2$ (D), while similar to that of samples used in several previous magnetic studies [2, 8, 15], is substantially higher than that of $LiNiO_2$ (X). This point may be particularly significant since it has been proposed by Hirota et al. [15] that such extended high temperature heating may result in the progressive loss of Li from the sample and lead to enhanced Ni/Li substitution. Thus, purely on the basis of preparation technique, one might expect that of the two samples studied in this experiment, $LiNiO_2$ (X) is likely to be closer to optimal stoichiometry and possess a lesser degree of ionic mixing. The interested reader is referred to Reimers et al. [6] for additional details regarding $LiNiO_2$

sample preparation[1].

The polycrystalline sample of $NaNiO_2$ used by Lewis et al. [1] was synthesized at McMaster University by Hanna Dabkowska and Israel Crooks. It was prepared from stoichiometric amounts of Na_2O_2 and NiO, which were mixed and formed into pellets in the presence of an Ar atmosphere. These pellets were then annealed in O_2 for 70 hours at 700C, with one intermediate grinding.

2.2 Sample Characterization

The low-field dc magnetic susceptibility of the three samples, χ(T), was measured using a Quantum Design MPMS SQUID magnetometer. Data was collected in the form of both zero field cooled (ZFC) and H=0.05T field cooled (FC) runs. The resulting dc susceptibilities of $LiNiO_2$ (X) and (D) are shown in figures 2.1 and 2.2 respectively. Note that for both samples, there is clearly a visible peak in χ(T), indicating the presence of a magnetic phase transition. There is a noticeable difference in the observed transition temperatures, with $T_g \sim 15$K in $LiNiO_2$ (X) and $T_g \sim 9$K in $LiNiO_2$ (D). Similarly, both samples exhibit a pronounced gap between the measured FC and ZFC susceptibilities. This form of history dependence and irreversibility provides evidence of "glassy" behaviour, extending from base temperature to ~ 50K and ~ 200K in samples (X) and (D) respectively. The fact that the gap between FC and ZFC susceptibilities increases in magnitude below T_g is consistent with spin glass freezing, suggesting that the observed phase transition at T_g is a glass transition. The difference in the magnitudes of the FC magnetizations of the two samples may be interpretted as an indication that the ferromagnetic interactions in $LiNiO_2$ (X) are stronger than those in $LiNiO_2$ (D).

---

[1] Note that throughout this reference the sample which we have labelled as $LiNiO_2$ (X) is described as $LiNiO_2$ (B).

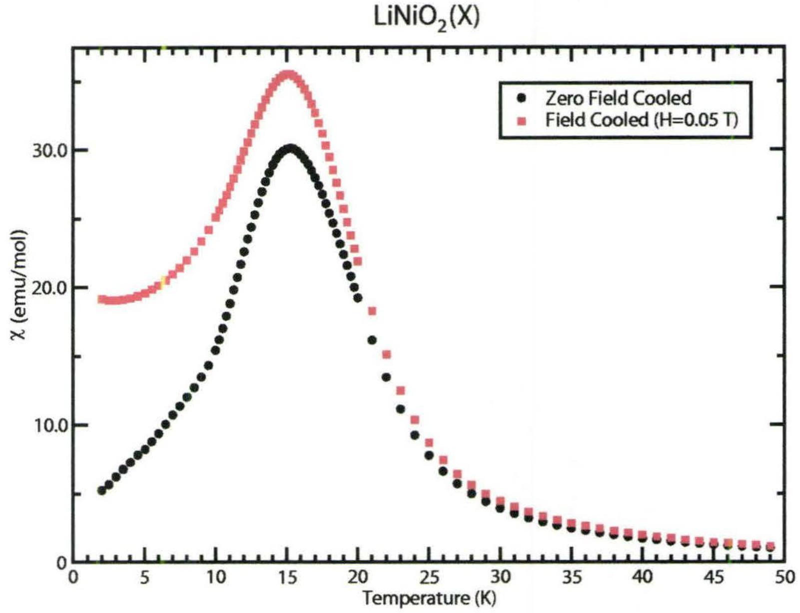

Figure 2.1: DC magnetic susceptibility of $LiNiO_2$ (X).

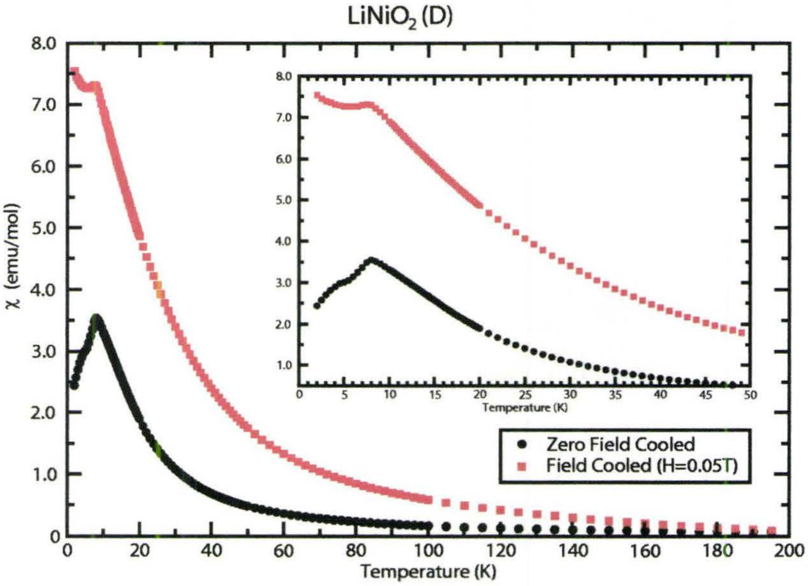

Figure 2.2: DC magnetic susceptibility of $LiNiO_2$ (D).

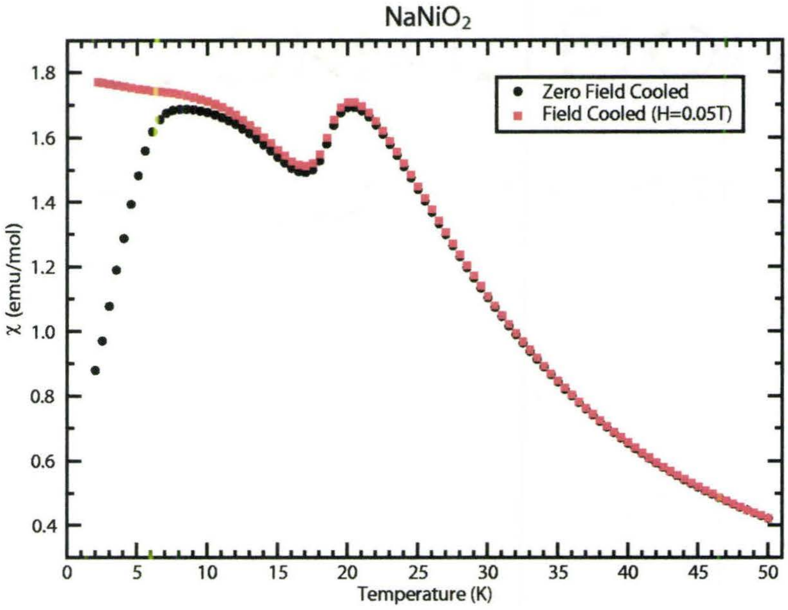

Figure 2.3: DC magnetic susceptibility of NaNiO$_2$.

In contrast, consider the plot of the dc magnetic susceptility of NaNiO$_2$ provided in figure 2.3. As before, we can observe that a peak in χ(T) provides evidence of a magnetic phase transition at $T_N \sim 23$K. Also note that a gap between FC and ZFC susceptibilities emerges below approximately 10K, signifying that at low temperatures a degree of glassiness exists within the magnetically ordered state of NaNiO$_2$. It is clear, however, both from the magnitude of the irreversibility and from its far smaller temperature range, that this glassy behaviour is far less dramatic than that observed in either of the LiNiO$_2$ samples.

The high temperature dc susceptibility of LiNiO$_2$ was fit to a Curie-Weiss law, as indicated in figure 2.4. The fit was performed using data collected over a temperature range of 220K to 300K, thus avoiding the non-linearities in magnetization which arise below $\sim$ 215K. The Curie-Weiss constants calculated for samples (X) and (D) were $\theta_X = +55(2)$K and $\theta_D = +40(2)$K respectively. It should be noted that

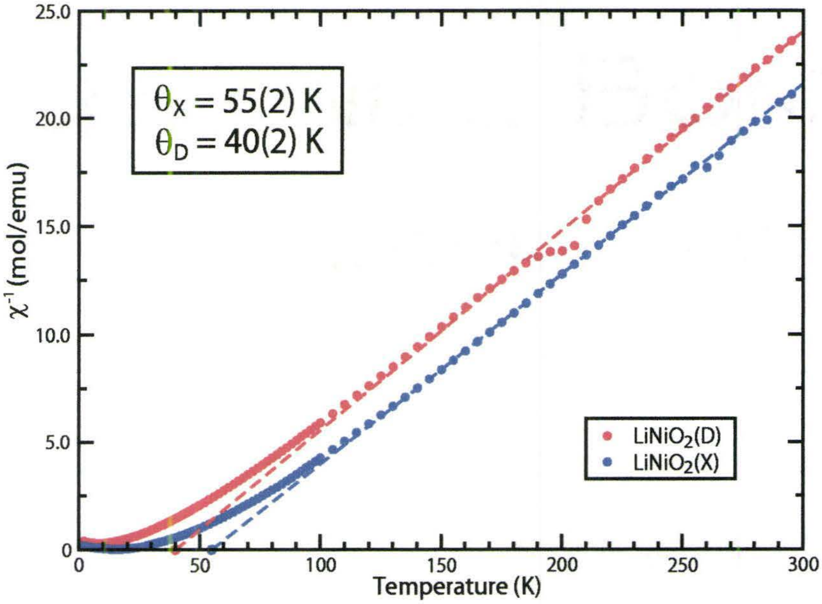

Figure 2.4: Curie-Weiss law fit to the magnetic susceptibility of LiNiO$_2$.

these values fall well within the range of previously reported Curie-Weiss constants, which extends from $\theta = -65(20)$K [2] to $\theta = +79(5)$K [15]. More importantly, however, both values are close to the predicted Curie-Weiss constant of stoichiometric LiNiO$_2$, which has been suggested to lie between +26K and +35K based on recent studies of high purity samples [25, 18, 13]. Since the Curie-Weiss constant is a measure of the average sum of the exchange interactions on an atomic site, the fact that θ is greater than zero signifies that the dominant correlations in LiNiO$_2$ (X) and (D) must be ferromagnetic in nature.

The stoichiometry of both of the LiNiO$_2$ samples used in this experiment was previously determined from x-ray powder diffraction data using the Reitveld method of structure refinement. These refinements were performed by Reimers et al. in 1993 [6] and by van Duijn et al. in 2001 [27]. The original assessment of sample stoichiometry by Reimers et al., indicated that samples (X) and (D) were

$Li_{1-x}Ni_{1+x}O_2$ with x_X = -0.02(1) and x_D = +0.03(1) respectively [6]. Thus, (X) was found to be slightly Ni deficient and (D) was found to be slightly Li deficient, with (X) being the closer of the two samples to ideal stoichiometry. An additional parameter, δ, was introduced to the model to account for the substitution of Li and Ni ions in the crystal structure. Refinements of δ revealed ionic mixing on the level of 1.5(3)% in (X) and 3.2(3)% in (D) [6]. The second structure refinement of $LiNiO_2$ (X), performed by van Duijn et al. nearly a decade later, suggested that the sample had a very different composition, one which was deficient in Li rather than Ni, with x_X = +0.029(1) [27]. A comparison of the dc magnetic susceptibility measurements which accompanied each structure refinement suggests that the present form of $LiNiO_2$ (X) is more appropriately described by the refinement of van Duijn et al., while $LiNiO_2$ (D) is still accurately represented by the initial refinement of Reimers et al[2].

2.3 Neutron Scattering Measurements

The neutron scattering experiments described in this thesis were carried out at the National Institute of Standards and Technology (NIST) Center for Neutron Research, a 20 MW research reactor located in Gaithersburg, Maryland. Measurements were performed using the Disk Chopper Spectrometer, or DCS, a direct geometry time-of-flight instrument, and currently the only instrument of its kind in North America[3]. The DCS is a cold neutron instrument, utilizing neutrons which are

---

[2] This is based on a comparison of the observed glass transition temperatures (T_g = 9K in 1993 compared to T_g = 15K in 2001) and the calculated Curie-Weiss constants (θ = 2(10)K in 1993 compared to θ = 61K in 2001).

[3] It should be noted, however, that the construction of three additional direct geometry time-of-flight spectrometers, CNCS, ARCS, and SEQUOIA, is nearing completion at the new Spallation Neutron Source in Oak Ridge, Tennessee.

produced by the reactor and then moderated to $\sim$ 20K by a liquid hydrogen cold source.

Before reaching the spectrometer, neutrons from the cold source pass through two filters which remove fast neutrons and gamma particles from the beam. They then travel through a system of seven choppers which are used to pulse and monochromate the incident neutrons, eliminate higher order wavelength contamination, and minimize the effects of frame overlap. Three slits of varying widths are cut into the pulsing and monochromating choppers, allowing the instrument to operate in three different resolution modes (high, medium, and low). The choppers typically rotate at a master speed of $\omega_0 = 20{,}000$ rpm or $\sim$ 333 Hz, with the exception of the frame overlap chopper which rotates at ω_0/m (where m is a chopper parameter referred to as the speed ratio). The incident beam is 10 cm tall, with a width that varies from 1 cm to 3 cm depending on the choice of resolution mode. An oscillating radial collimator is used to reduce scattering from the cryostat and other sample environment structures.

After interacting with the sample, scattered neutrons are counted by an array of 913 ^{3}He detectors. The detectors are arranged in 3 banks, which cover a range of scattering angles extending from -30° to -5° and 5° to 140°. The distance from the sample to the detectors is 4.010 m. The detectors are housed in an Ar-filled flight chamber which minimizes the effect of air scattering along the neutron flight path. By applying standard time-of-flight techniques, the time and position of every counted neutron can be used to determine both the transfer of energy and momentum which occurred during each scattering event. A labelled schematic of the DCS is provided in figure 2.5. For a more detailed description of the instrument and its technical specifications, the reader is referred to a recent publication by Copley and Cook [29].

There are four chopper parameters which must be carefully selected for any experiment on the DCS. These include the incident wavelength, λ, the resolution

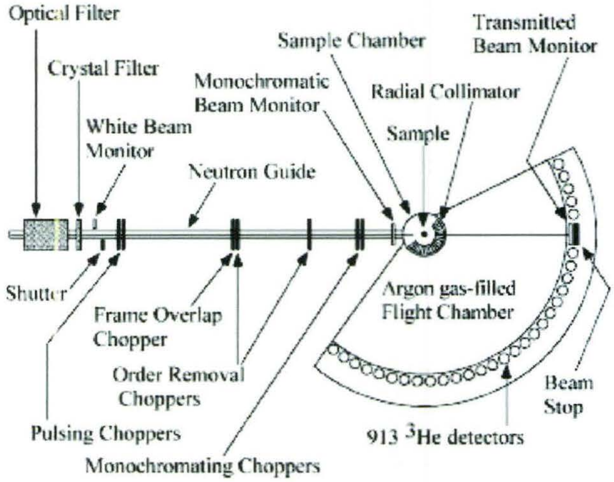

Figure 2.5: Schematic of the Disk Chopper Spectrometer (DCS) [Courtesy of J.R.D. Copley and J.C. Cook (2003) [29]].

mode, r, the speed ratio, m, and the time delay, t_{SD}(min). The choice of these parameters determines critical details such as the accessible range of energy and momentum transfer, the frequency and intensity of the incident beam, and the resolution in E and Q. The effect of r and λ on the intensity of the incident beam and the resolution of the instrument is illustrated in figures 2.6 and 2.7 respectively. In both the $LiNiO_2$ and $NaNiO_2$ experiments, measurements were performed in the low resolution mode of operation, with an incident wavelength of $\lambda = 5.5$ Å. For this choice of r and λ the intensity of the neutron beam at the sample position is 6.46×10^5 neutrons/s, the flux is 3.23×10^5 neutrons/cm^2/s, and the energy resolution of the instrument is 0.081 meV for the elastic scattering regime.

The speed ratio parameter, m, which is chiefly responsible for the elimination of frame overlap, was set to 2. With $m = 2$ the pulse frequency of the incident beam is approximately 167 Hz and the time interval between each pulse is 6000 μs. The delay time, T_{SD}(min), was chosen to be 3500 μs. This restricted the range of measureable

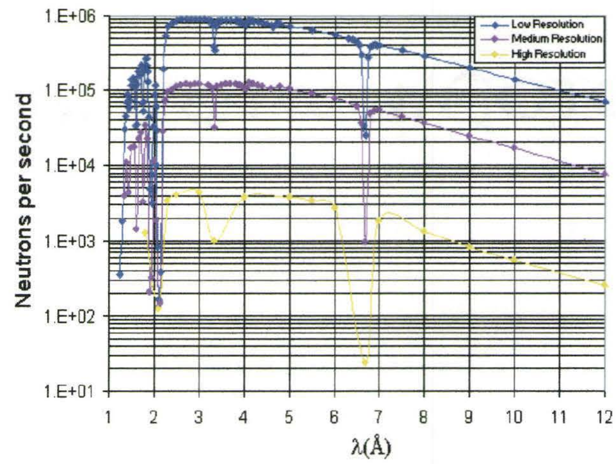

Figure 2.6: Neutron intensity (at sample) as a function of wavelength for the DCS [Courtesy of DCS User's Guide [30]].

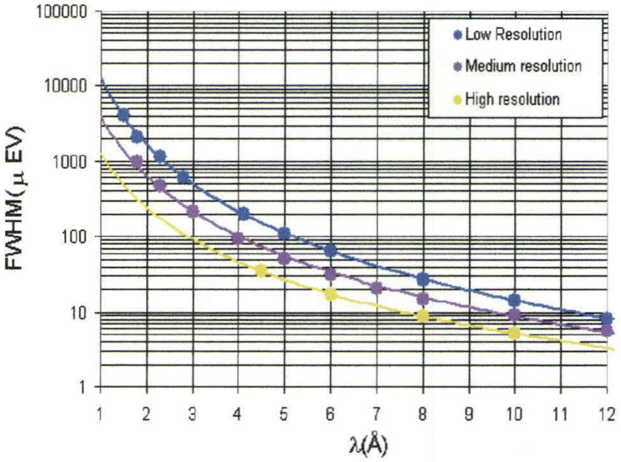

Figure 2.7: Elastic energy resolution as a function of wavelength for the DCS [Courtesy of DCS User's Guide [30]].

final neutron energies to between 0.93 meV and 6.8 meV. The kinematically accessible region of energy and momentum space defined by this set of chopper parameters is shown in figure 2.8.

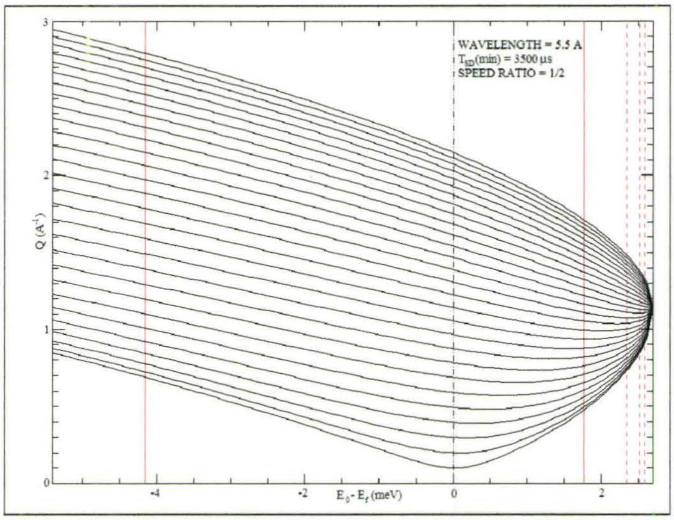

Figure 2.8: Kinematically accessible region for $\lambda = 5.5$ Å, $m = 2$, and $t_{SD}(\text{min}) = 3500$ μs.

Measurements were performed on polycrystalline samples of $LiNiO_2$ (X) and (D) with masses of 22 g and 28.5 g respectively. Due to the anticipation of absorption problems caused by the presence of ^{6}Li, the samples were mounted in aluminum cans designed with a thin annular geometry. These cans were 10 cm in height, having an annular sample thickness of 0.635 cm and an outer wall with an inner diameter of 1.27 cm. The $NaNiO_2$ sample consisted of 30 g of powder material pressed into the form of a rod. The sample was wrapped in Al foil, then secured in a cylindrical aluminum can. The loading of all three samples was performed in the presence of helium exchange gas to ensure proper thermal contact with the system.

The sample environment was provided by a 70mm ILL "orange" cryostat, designed with an operating range of temperatures from 1.4K to 300K. $LiNiO_2$ data was collected at 11 different temperatures for each sample, ranging from base (T = 1.7K) to approximately 4 × T_g (T = 60K). The counting times varied from between 4 to 6 hours per temperature. $NaNiO_2$ measurements were performed at 8 different temperatures, running from base temperature (T = 5.5K) to approximately 2 × T_N (T = 50K). Counting times for $NaNiO_2$ ranged from 5 to 15 hours per temperature.

Chapter 3

Analysis and Results

In this chapter I will describe the analysis of our $LiNiO_2$ and $NaNiO_2$ neutron scattering data, and discuss several of the interesting experimental results which emerged from our measurements. I will begin with a brief discussion of the methods which have been used to analyze the data, with a particular emphasis on the determination of an appropriate background correction. This will be followed by a comparison of the elastic and inelastic scattering measurements collected for both materials, with an explanation of what this information can reveal regarding the structure and dynamics of these two systems.

3.1 Background Subtractions and Corrections

The most challenging aspect of the analysis performed in this study involved the process of developing a suitable method of background subtraction for the raw data. After a period of extensive experimentation, what is believed to be the optimal solution was achieved by applying a combination of four different forms of background correction. The first of these corrections was performed to normalize detector efficiency. This was accomplished using a vanadium run, a set of measurements collected with a cylindrical sample of vanadium in the beam. Due to its remarkably high incoherent cross section (5.19 barns/atom) and low coherent cross section (0.02 barns/atom), the scattering from vanadium is almost perfectly isotropic. This makes vanadium runs an ideal method of measuring relative detector efficiency of an instrument. It should be noted that the vanadium runs used for detector normalization were performed several weeks prior to the $LiNiO_2$ and $NaNiO_2$ experiments. While this had no noticeable effect on the quality of the $LiNiO_2$ data, it is almost certainly responsible for an arc of anomalously low scattering intensity, corresponding to a single low efficiency detector, which is visible in the $NaNiO_2$ data.

A second correction was applied to the data to account for scattering from the surrounding sample environment, and in particular, to compensate for scattering due to the aluminum sample can. This can be accomplished with the aid of an empty can run, a standard scan which is performed with an empty aluminum can and no sample in the beam. In principle, the scattering contribution from the sample environment can be removed by carrying out a simple subtraction of the form $I_{sample} = I_{sample+can} - I_{can}$, leaving only the scattering contribution from the sample itself.

The empty can subtraction described above becomes far more complicated in the presence of a strongly absorbing sample like $LiNiO_2$. In this type of situation, it is possible for the sample to effectively block or screen the far side of the aluminum can from the incident neutrons, reducing the overall scattering contribution made by the can. Thus, for absorbing samples, the empty can subtraction tends to provide an overestimate of the effect of the sample environment. This phenomenon, known as self-shielding or self-absorption, leads to the need for a third correction to the raw data. This correction simply involves the addition of a weighting factor, ss, to the empty can subtraction. Hence, with the inclusion of a self-shielding correction, our previous expression for the empty can subtraction merely becomes $I_{sample} =$

$I_{sample+can} - ss \times I_{can}$.

Unfortunately, determining the proper value of the self-shielding factor is often less than trivial, especially since the calculations required for an absorption correction have no analytical solution for samples with cylindrical or annular geometries [31]. Given the appropriate scattering and absorption cross sections, the dimensions of the sample and can, the size of the incident beam, and the characteristics of the radial collimator, it is possible to determine a theoretical value of ss numerically. The results of such a numerical calculation, performed using the Data Analysis and Visualization Environment (DAVE) developed by the NIST Center for Neutron Research, are provided in figure 3.1. The average value of ss over the range of scattering angles covered by the DCS is ~ 0.245, indicating that approximately three-quarters of the scattering from the sample environment is effectively shielded by the sample.

It should be noted that the self-shielding correction performed in DAVE is not a perfect solution, but merely an approximation. While the true self-shielding factor varies as a function of the scattering angle, 2θ, as shown by the calculations in figure 3.1, the current software will only permit a correction based on the average value of ss. Specifically, this means that the $|Q|$ dependence of the self-shielding correction is inaccurate, resulting in an oversubtraction of the empty can being performed at low $|Q|$ and an undersubtraction being performed at high $|Q|$. For $NaNiO_2$, which has a relatively small absorption cross section, no self-shielding correction was required during the analysis of the data (i.e. the appropriate self-shielding factor was $ss = 1$).

The final correction made to the data was the subtraction of a background scattering function. The need for this correction became apparent during the analysis of the inelastic scattering, which revealed the presence of a $|Q|$-independent background which varied exponentially as a function of the sample energy trans-

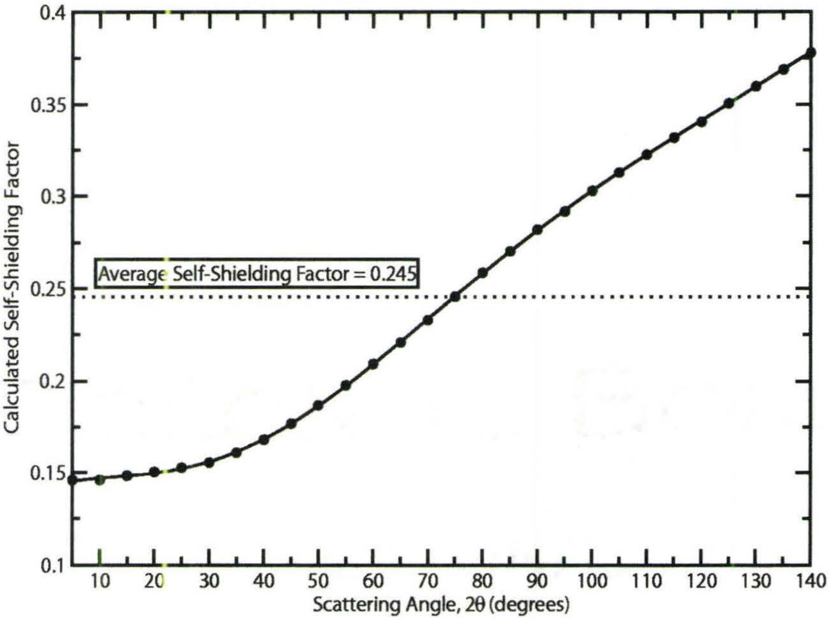

Figure 3.1: Calculated values of the self-shielding factor for $LiNiO_2$. The average self-shielding correction, $ss = 0.245$, is indicated by a dotted line.

fer, E. This same form of background scattering was previously observed in several other DCS experiments, including recent studies of $Ho_2Ti_2O_7$ and $Tb_2Ti_2O_7$ [32]. The exact form of the exponential background was determined by fitting the scattering at large negative energy transfers (-4 meV $< E <$ -1 meV) for the lowest temperature dataset. Since the principle of detailed balance demands that there be no real scattering intensity in this region at low temperatures, any signal must be the result of the background function. In $LiNiO_2$, this background was fit to $I_{background} = 0.014(4) + 0.079(4) \times e^{0.82(4)E}$. As a possible indication of the validity of this correction, the same results were yielded by two independent fits performed on the base temperature datasets of both $LiNiO_2$ (X) and (D). Applying a similar procedure to the large negative energy transfer regime in $NaNiO_2$ revealed an exponential background described by $I_{background} = 0.032(4) \times e^{0.94(6)E}$.

A comparison of several different forms of background subtraction is provided in figure 3.2, highlighting the difficulties created by strong sample absorption. With no background subtraction, the raw data clearly shows strong background scattering, particularly at large positive energy transfers and in the low $|Q|$ region. While the empty can subtraction resolves the problem of the exponential background function, it also creates a large region of negative scattering intensity in the elastic channel. As scattering intensity less than zero is unphysical, this form of correction must be disregarded. For similar reasons, the base temperature data subtraction is also unsatisfactory. Here, however, there is not only a negative signal in the elastic channel but also a violation of detailed balance, as the scattering for negative energy transfer (sample energy loss) outweighs that of positive energy transfer (sample energy gain). By combining the empty can subtraction with a self-shielding correction, we can maintain a positive intensity in the elastic channel while considerably reducing the background at large, positive E. This correction is not ideal, as it still requires the subtraction of the exponential background function described above, but it has the benefit of being both physically reasonable and theoretically justified.

3.2 Elastic Scattering Results

We begin our discussion of the experimental results with an examination of the elastic scattering data. As mentioned in section 2.1, elastic scattering measurements reveal information which describes the structure and static behaviour of a system. As the focus of this study is primarily concerned with the magnetic properties of $LiNiO_2$ and $NaNiO_2$, it is specifically the magnetic contribution to the elastic scattering which will be of interest to us. By taking advantage of the relatively weak temperature dependence of nuclear scattering, we can effectively isolate the magnetic signal by subtracting a high temperature dataset collected above the magnetic phase transition.

A plot of the elastic magnetic scattering measured in $NaNiO_2$ is provided in figure 3.3. Here the subtraction of a dataset at T = 50K ($\sim 2 \times T_N$) has been used to eliminate the contribution of nuclear scattering. This plot clearly shows the development of two magnetic Bragg peaks below the magnetic phase transition at $T_N \sim 23$K. These two peaks, located at $|Q| \sim 0.59$ $\mathring{A}^{-1}$ and $|Q| \sim 1.21$ $\mathring{A}^{-1}$, can be indexed as (0,0,1/2) and (0,0,1) respectively. The appearance of the (0,0,1/2) peak is particularly significant, since it implies a doubling of the magnetic unit cell along the direction of the *c*-axis due to a π phase shift between the magnetic moments of Ni ions on neighbouring triangular planes.

It is worth noting that during the original analysis of the $NaNiO_2$ data it was a comparison of the relative intensities of these and other magnetic Bragg peaks that allowed Lewis et al. [1] to determine the structure of the magnetically ordered

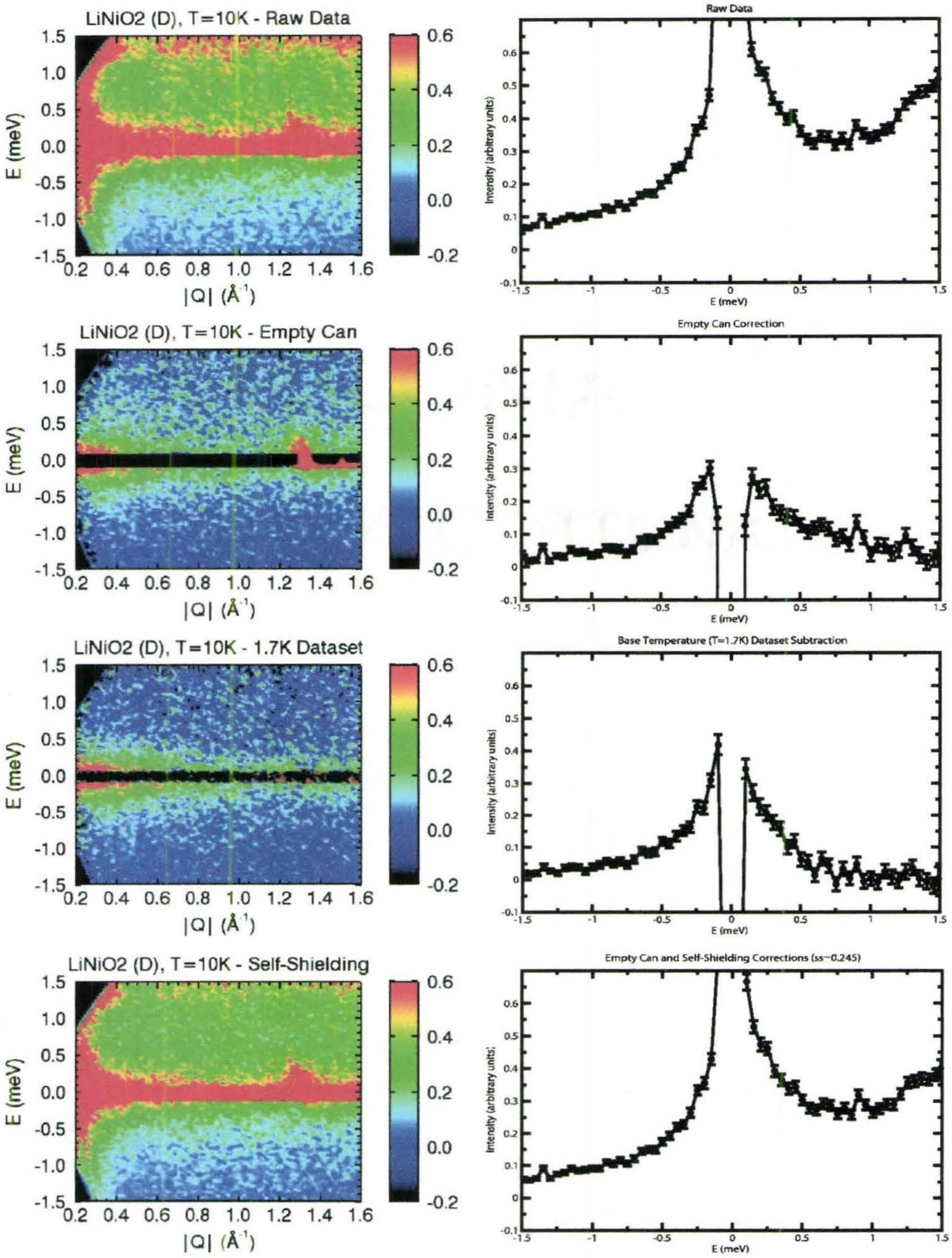

Figure 3.2: Possible background corrections for $LiNiO_2$. Pictured here are E vs. $|Q|$ slices and energy cuts for the T = 10K dataset of $LiNiO_2$ (D) with four different background corrections. From top to bottom they are: uncorrected raw data, empty can subtracted data, base temperature (T = 1.7K) subtracted data, and empty can subtracted data with self-shielding correction ($ss = 0.245$).

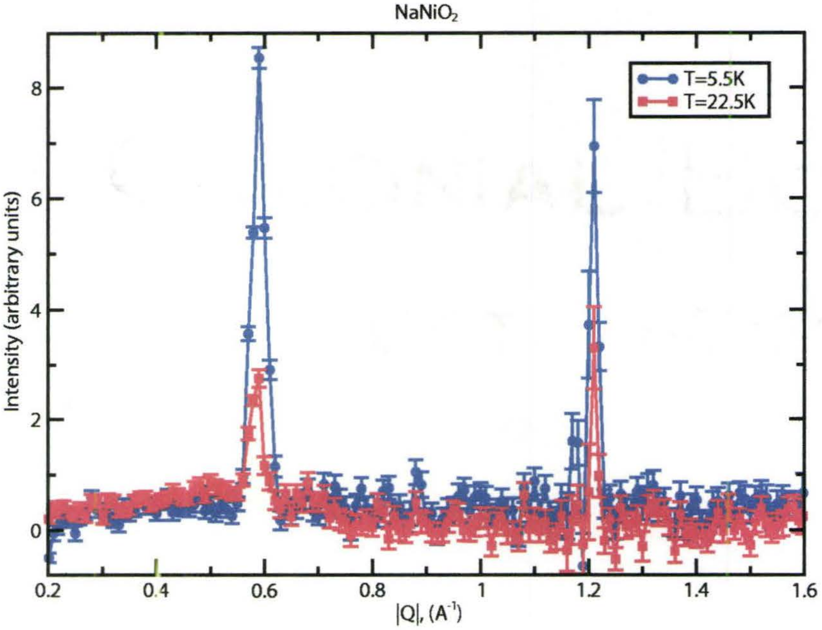

Figure 3.3: Elastic magnetic scattering in NaNiO$_2$. The peaks at $|Q| \sim 0.59$ $\mathring{A}^{-1}$ and $|Q| \sim 1.21$ $\mathring{A}^{-1}$ correspond to the (0,0,1/2) and (0,0,1) magnetic Bragg peaks which appear below T$_N$ ~ 23K. Subtraction of the T = 50K dataset has been performed to eliminate the contribution of nuclear scattering.

state below T$_N$. This result, consistent with the magnetic structure first proposed by Bongers and Enz in 1966 [26], suggests that the magnetically ordered state of NaNiO$_2$ consists of antiferromagnetically stacked layers of ferromagnetically aligned spin 1/2 moments.

The integrated intensity of the (0,0,1/2) magnetic Bragg peak is plotted as a function of temperature in figure 3.4. These intensities were determined by fitting the (0,0,1/2) peak shape to a Gaussian fit function. Since the intensity of a magnetic Bragg peak is proportional to $\langle S\rangle^2$, the square of the order parameter, the behaviour of the integrated intensity can convey valuable physical information about the nature of the system. Specifically, the fashion in which the integrated intensity tends to zero

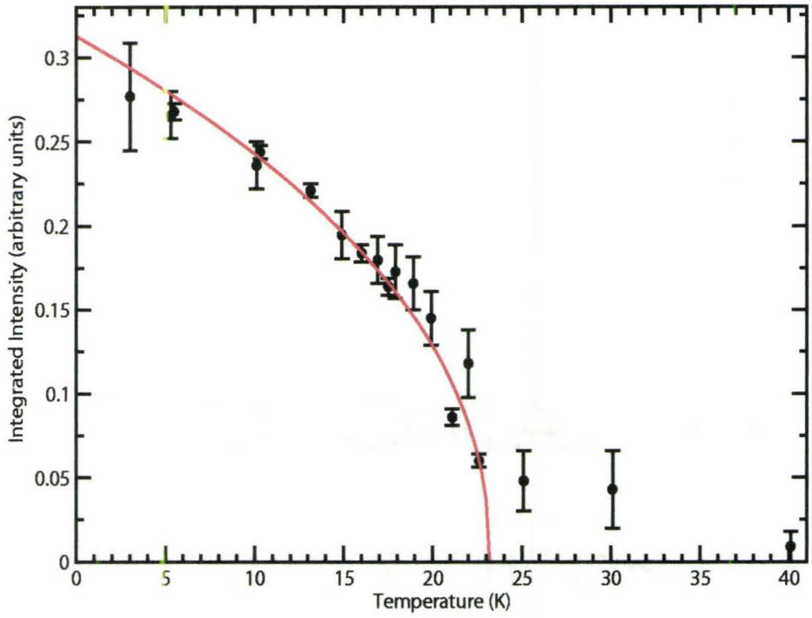

Figure 3.4: Integrated intensity of the (0,0,1/2) magnetic Bragg peak in $NaNiO_2$. A power law fit to the data is provided in red.

near T_N indicates that the magnetic phase transition in $NaNiO_2$ is continuous. The intensity of the (0,0,1/2) peak can be fit to a power law of the form $I = A \times \left(\frac{T_N - T}{T_N}\right)^{2\beta}$, as illustrated by the red curve in figure 3.4. The parameters determined from this fit were A = 0.313(6), $T_N = 23.2(1)$K, and $\beta = 0.23(2)$. Given the low density of points measured in the immediate vicinity of T_N, one must be cautioned not to put too much emphasis on the value of the critical exponent β. However, it is intriguing to note that our fitted value of $\beta = 0.23(2)$ does fall within the range of the theoretically predicted critical exponents for both mean field theory tricritical behaviour, $\beta = 0.25$ (exact) [33], and the XY triangular antiferromagnet, $\beta = 0.25(2)$ [34]. At the very least, it seems likely that the relatively low value measured for β reflects the quasi-two dimensional behaviour of the system.

A very different picture emerges from a study of the elastic scattering in

$LiNiO_2$. Consider the plot of the observed magnetic elastic scattering from $LiNiO_2$ (X) which is provided in figure 3.5. As before, a high temperature dataset collected at T = 60K ($\sim 4 \times T_g$) has been subtracted to account for the effect of nuclear scattering. This figure clearly indicates that there remains a lack of either magnetic or orbital long range order down to temperatures as low as T = 1.7K. This result is consistent with the previous neutron studies of Hirakawa et al. [2] and van Duijn et al. [27]. The absence of long range magnetic ordering is demonstrated by the fact that no new magnetic Bragg peaks appear below the transition temperature, $T_g \sim$ 15K. Similarly, the absence of long range orbital ordering can be inferred from the lack of any new structural Bragg peaks below T_g, which one might expect to arise due to the lattice distortion which accompanies a cooperative Jahn-Teller distortion. It is important to note that due to a lack of temperature dependence between 1.7K and 30K the visible peak at $|Q| \sim 1.34$ $\AA^{-1}$ can be disregarded as either a new structural or magnetic peak. Instead, it is most likely the result of mismatching of the (0,0,1) Bragg peak caused by a slight change in the *c*-axis lattice parameter between the low temperature datasets and the 60K background.

Below $T_g \sim$ 15K, the measurements in Figure 3.5 also show the development of broad magnetic scattering in the low-$|Q|$ region, from approximately 0 to 0.6 $\AA^{-1}$. The fact that this diffuse elastic scattering appears to peak near $|Q| = 0$ is another indication, like the suceptibility data presented in chapter 3, that the dominant correlations in $LiNiO_2$ must be ferromagnetic. The broadness of the magnetic scattering is also significant, since it implies that the nature of these correlations must be very short-ranged.

Another interesting trend emerges from an examination of the integrated intensity of the elastic scattering, as shown in figure 3.6. Here the elastic signal, represented by the closed circles, has been integrated over energy transfers from -0.1

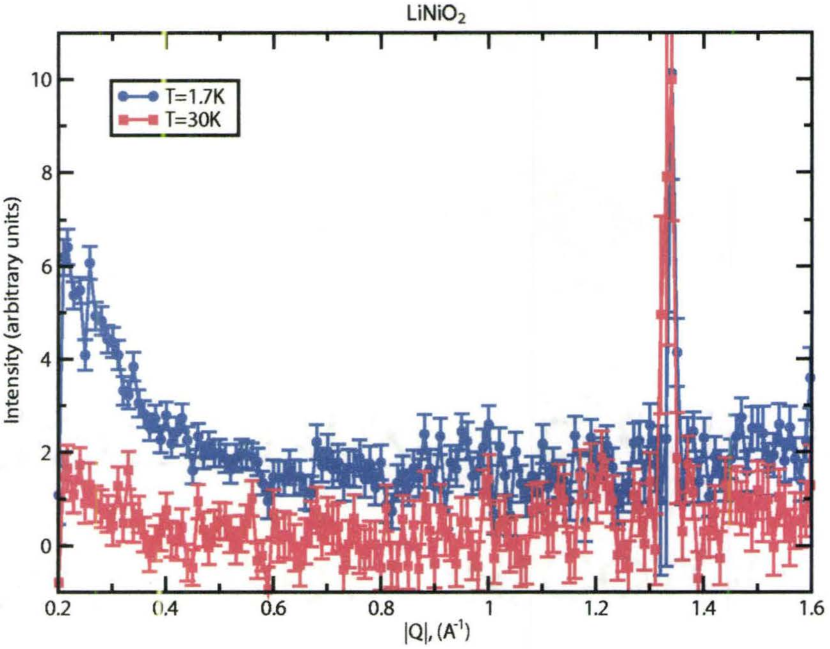

Figure 3.5: Elastic magnetic scattering in LiNiO$_2$ (X). Broad magnetic scattering develops in the low $|Q|$ region below T$_g$ $\sim$ 15K, however there is no evidence of magnetic Bragg peaks. Subtraction of the T = 60K data set has been performed to eliminate the contribution of nuclear scattering.

to +0.1 meV and a range of $|Q|$ from 0.4 to 1.1 $\mathring{A}^{-1}$. For the purpose of comparison, this plot also includes the integrated intensity of the inelastic signal, represented by the open squares, which has been measured over energy transfers from +0.2 to +1.0 meV and the same range of $|Q|$. Notice that in the case of both $LiNiO_2$ (X) and (D), as the temperature drops below ~ 10K there is a marked decrease in the intensity of the inelastic signal accompanied by a simultaneous increase in the magnitude of the elastic signal. This form of behaviour is typical of what one might expect from a spin glass. At high temperatures, the majority of the spins in the sample are dynamic and free to fluctuate, giving rise to strong inelastic scattering. As the temperature of the sample drops towards T_g, the motion of the spins will become gradually slower, until ultimately spin freezing will begin to occur. As a growing number of spins become static, there will be both a significant increase in the intensity of the elastic signal and a corresponding decrease in the magnitude of the inelastic signal. From the data in figure 3.6 this appears to be precisely what occurs at $T_g \sim 10K$ in the case of $LiNiO_2$. Despite a ~ 6K difference between the values of T_g determined from the susceptibility measurements described in chapter 2, the temperature dependence of the integrated intensity of the two samples is almost indistinguishable. This apparent discrepancy almost certainly arises from the fact that dc susceptibility and neutron scattering measurements are sensitive to two very different time scales. While dc susceptibility measurements describe processes which occur over what is effectively an infinitely slow period of time, the information conveyed by neutron scattering measurements is associated with a comparitively rapid time scale, typically on the order of $\sim 10^{-10}$ seconds. As a result, what appears to be static behaviour for one technique does not necessarily need to appear static for the other.

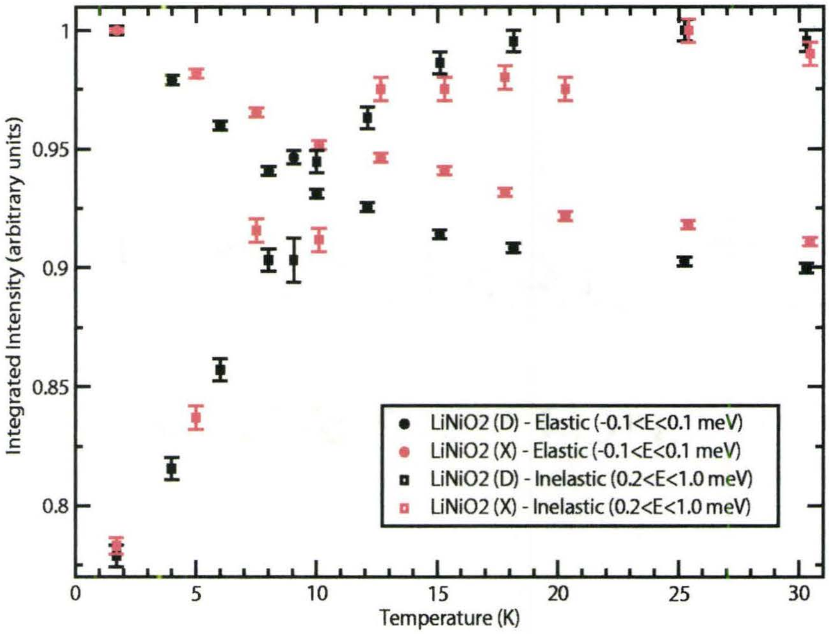

Figure 3.6: Integrated elastic and inelastic scattering intensity in $LiNiO_2$ (D) and (X). The elastic and inelastic scattering are represented by closed circles and open squares respectively. Data from sample (D) is shown in black, while data from sample (X) is provided in red. Intensities have been normalized for comparative purposes.

3.3 Inelastic Scattering Results

As illustrated in the previous section, elastic scattering measurements can be used as an effective tool to determine details related to the structure and static properties of materials. However, in order to obtain information concerning the excitations and dynamics of a system, it is necessary to examine the features of the inelastic scattering. The time-of-flight measurements which can be performed on the DCS are a particularly effective method of studying inelastic scattering, since they allow extremely rapid collection of scattering information from a wide range of energy and momentum transfers. As a result, it is possible to map out the dispersion relations of a system very quickly in the form of E vs. $|Q|$ slices.

Several representative E vs. $|Q|$ slices for $NaNiO_2$ are provided in figure 3.7. These slices were collected at four temperatures ranging from base (T = 5.5K) to just below the magnetic phase transition at T_N (T = 22.5K). At low temperatures, the slices provide clear evidence of two different inelastic excitations. The first of these excitations is a spin wave, or magnon, which is visible as a curved inelastic feature near low $|Q|$. The spin wave reaches a maximum energy of E $\sim$ 0.8 meV near the zone boundary at $|Q| \sim 0.3$ $\mathring{A}^{-1}$ and approaches zero energy at the (0,0,1/2) magnetic zone center located at $|Q| \sim 0.59$ $\mathring{A}^{-1}$. The second excitation is a flat, dispersionless inelastic mode found at E $\sim$ 0.8 meV. While weaker in intensity than the spin wave, this dispersionless feature stretches across the entire range of measured $|Q|$.

These two inelastic modes are also clearly visible in energy cuts taken through the data, as shown in figure 3.8. The two cuts displayed in this plot were taken from the T = 10K dataset and performed over $0.49 < |Q| < 0.51\mathring{A}^{-1}$ and $0.79 < |Q| < 0.81\mathring{A}^{-1}$ respectively. At $|Q| \sim 0.5$ $\mathring{A}^{-1}$, the energy cut shows four distinct peaks. The two peaks at ± 0.4 meV correspond to the spin wave mode, while those at ± 0.8 meV are associated with the dispersionless mode. Further out in $|Q|$, at $\sim$ 0.8

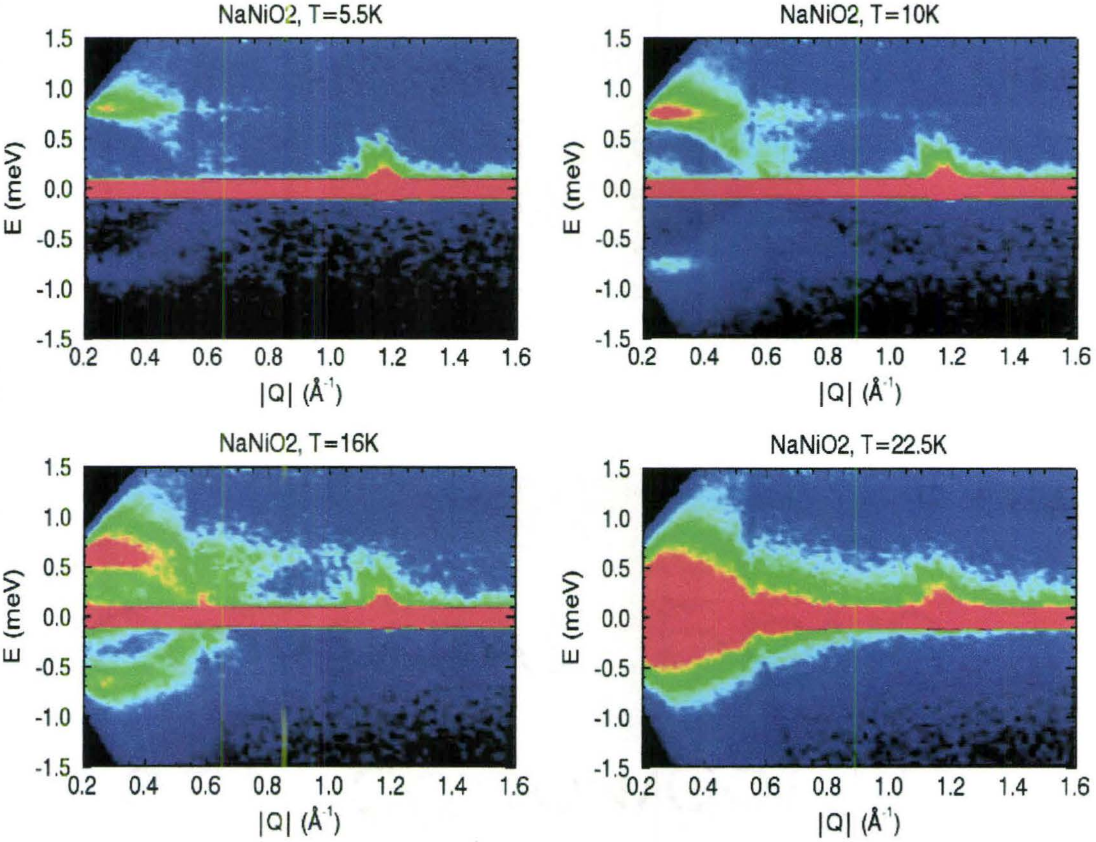

Figure 3.7: Representative data for $NaNiO_2$. Shown here are E vs. $|Q|$ slices collected at T = 5.5K, 10K, 16K and 22.5K (~ T_N).

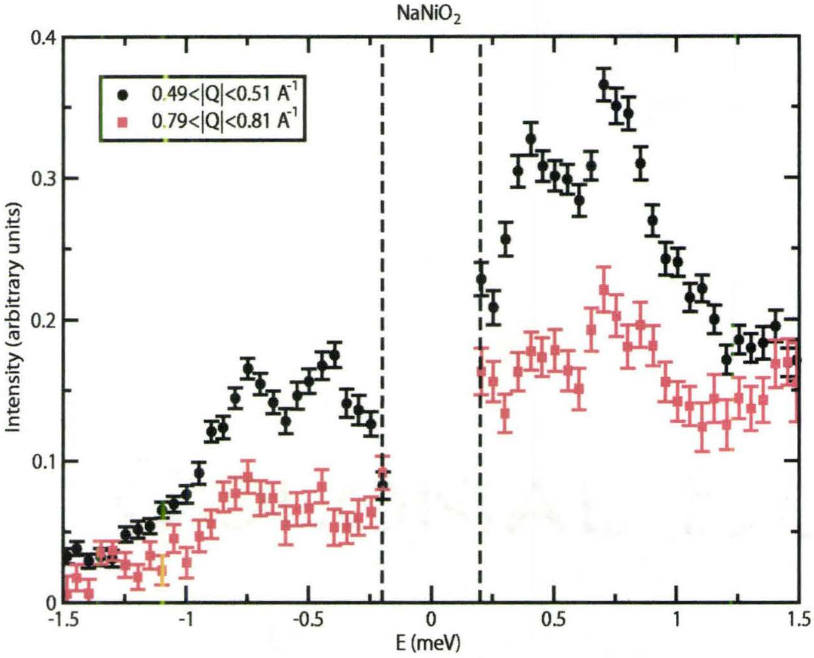

Figure 3.8: Representative energy cuts for $NaNiO_2$ at T = 10K. These two cuts, performed at $|Q| \sim 0.5$ Å^{-1} and 0.8 Å^{-1} respectively, show peaks corresponding to both the dispersionless mode at ± 0.8 meV and the spin wave mode at ± 0.4 meV.

$\mathring{A}^{-1}$, the only distinguishable peaks are those of the flat mode at ± 0.8 meV. Note that in both the energy cuts and the E vs. $|Q|$ slices, each of the inelastic excitations can be observed for either positive or negative energy transfers. The intensity of the signal on the negative E side of the inelastic spectrum is consistently weaker than the intensity on the positive E side. This is due to the fact that the scattering associated with sample energy loss (i.e. E < 0) is suppressed by the principle of detailed balance at low temperatures[1].

As the temperature of the system increases towards T_N, a marked change

---

[1] A second contribution to the apparent asymmetry also arises from the exponential background function described in section 4.1, although this is typically a less significant effect than detailed balance, particularly when the temperature is sufficiently low.

in the inelastic scattering occurs. At approximately T = 16K, both the spin wave and the dispersionless modes start to soften, and additional inelastic intensity begins to develop within the envelope of the spin wave dispersion. By T = 22.5K, the two inelastic modes have softened completely and collapsed. What remains of the spin wave envelope has been entirely filled by new inelastic scattering, and the magnetic order of the system has been almost totally destroyed. The evolution of the inelastic scattering as the system approaches T_N is illustrated by the sequence of representative slices in figure 3.7.

As noted by Lewis et al. [1], the presence of spin wave softening along the c-axis direction suggests that the phase transition at $T_N \sim 23$K corresponds to a loss of registry between adjacent layers of ferromagnetically ordered spin 1/2 moments. Thus, it appears to be disruptions of the antiferromagnetic correlations between planes, rather than the ferromagnetic correlations within the planes, which are responsible for the destruction of the magnetically ordered state in $NaNiO_2$. One consequence of this result is that the type of magnetic structure observed in $NaNiO_2$ is likely to be extremely vulnerable to the effects of stacking sequence frustration.

To provide a more quantitative description of the inelastic scattering in $NaNiO_2$, fits were performed to a series of energy cuts taken at $|Q| \sim 0.5$ $\mathring{A}^{-1}$ for a range of temperatures extending from base (T = 5.5K) to just below T_N (T = 22.5K). The inelastic spectrum was modelled using a combination of damped harmonic oscillator (DHO) functions of the form: $I(E) = N(E,T) \times \frac{A\Gamma}{\Pi} \times \left[\frac{1}{(E-E_0)^2+\Gamma^2} - \frac{1}{(E+E_0)^2+\Gamma^2}\right]$. Here the parameter A is the amplitude of the function, Γ is the half-width at half-maximum (HWHM), E_0 is the center of each Lorentzian component, and N(E,T) is the Bose thermal population factor, defined as $N(E,T) = \frac{1}{1-e^{-E/kT}}$. For $T \leq 16$K, where the energy cuts display distinct sets of peaks for each of the two inelastic modes, fits were performed using a two DHO fit function. For $T \geq 21$K, where the energy cuts show only a single broad peak centered at E $\sim$ 0, fits were performed to a one DHO fit function. At T = 17.5K, where the crossover between the two regimes occurs, fits were performed with both one and two DHO fit functions. Also included in the fit functions was a temperature independent exponential background function of the form discussed in section 4.1.

As demonstrated by the representative fits provided in figure 3.9, The DHO model describes the inelastic data quite well. The energy cuts displayed in this figure correspond to T = 5.5K, T = 10K, T = 16K, and T = 22.5K. This is the same set of temperatures used for the representative E vs. $|Q|$ slices shown in figure 3.7. A study of the inelastic fit parameters, and in particular the behaviour of the peak position and width as a function of temperature, can reveal valuable information regarding both the magnitude and life-time of the excitations in the system. A plot of the temperature dependence of the inelastic peak position is provided in figure 3.10. The center of an inelastic peak, E_0, corresponds to the magnitude of the energy associated with a given excitation. Figure 3.10 shows that in $NaNiO_2$, as the temperature of the system increases, the position of the two inelastic excitations gradually moves towards lower energies. This is equivalent to the softening of modes which was mentioned in the discussion on the previous page. Note that as the temperature approaches T_N, the softening of the modes becomes much more pronounced, ultimately leading to a complete collapse between 17.5K and 21K when the energy of both excitations drops to zero. The fact that the behaviour of the inelastic peak positions so closely resembles that of the magnetic Bragg peak intensity (shown in figure 3.3) forms another important link between the presence of mode softening and the magnetic phase transition at T_N.

The temperature dependence of the inelastic width parameter is shown in figure 3.11. The width parameter, or HWHM, of the inelastic peak, Γ, is proportional

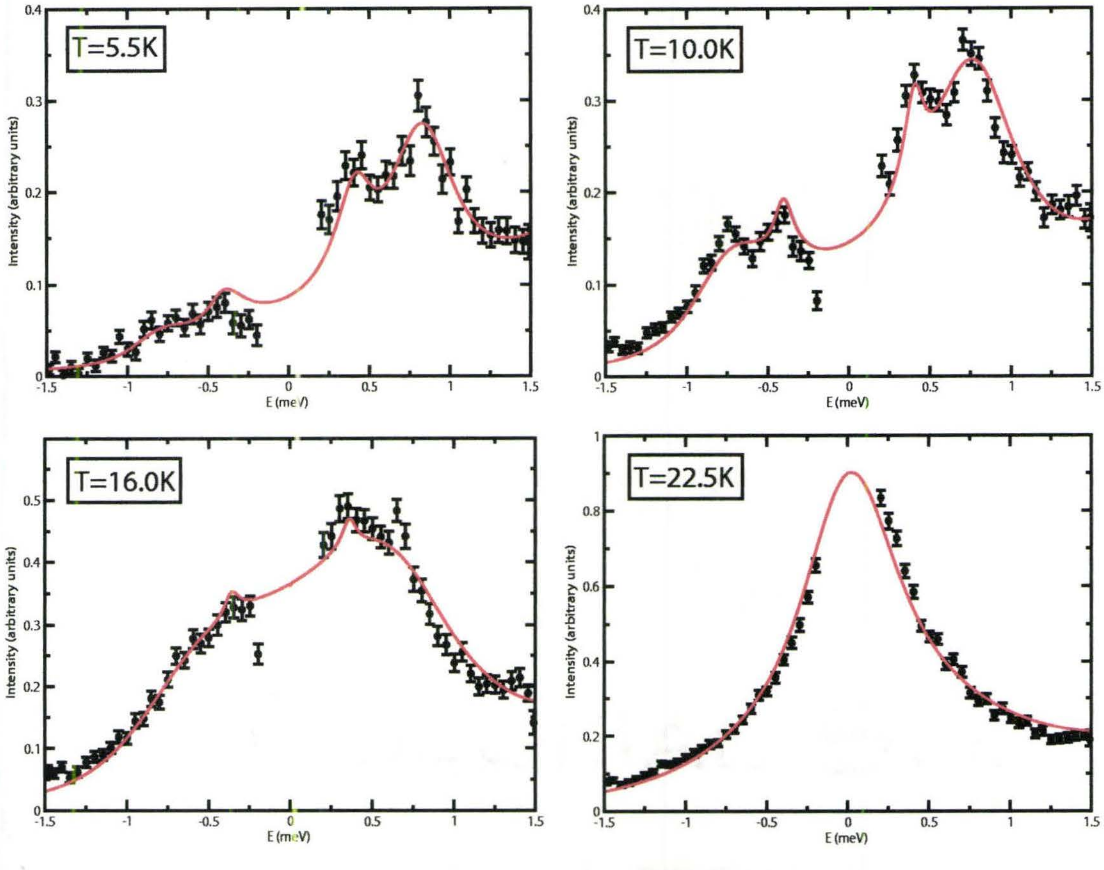

Figure 3.9: Representative fits of the inelastic spectrum in $NaNiO_2$. Energy cuts were performed at $|Q| \sim 0.5\ \mathring{A}^{-1}$.

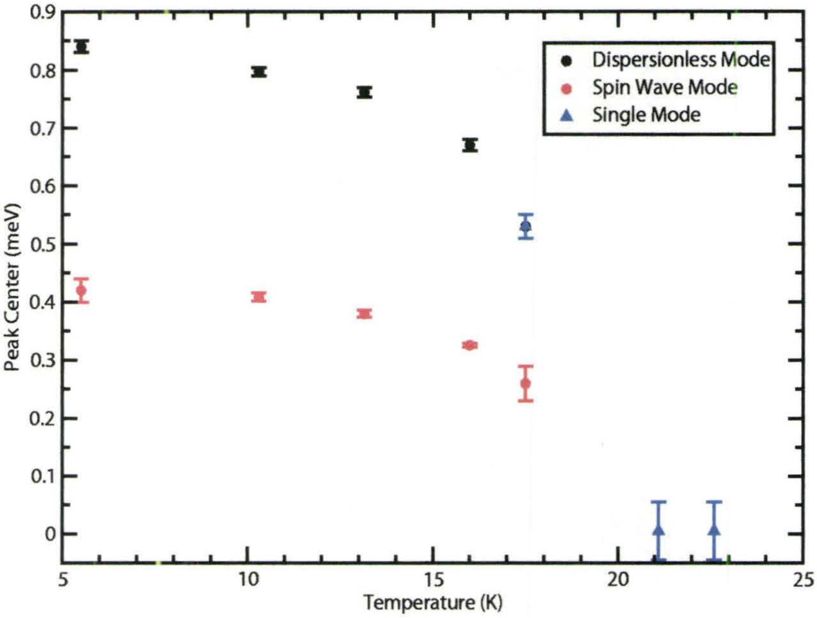

Figure 3.10: Inelastic peak position as a function of temperature in $NaNiO_2$.

to $1/\tau$, where τ represents the lifetime of the excitation. Therefore, a comparison of the relative peak widths of the two inelastic modes in figure 3.11 indicates that the spin wave mode has a significantly longer lifetime than the much broader dispersionless mode. Similarly, as the temperature of the system approaches T_N, the widths of the inelastic peaks appear to increase dramatically, indicating that the excitations are becoming much more short-lived in nature.

We now turn to a discussion of inelastic scattering measurements on $LiNiO_2$. Representative E vs. $|Q|$ slices for both $LiNiO_2$ (D) and (X) are provided in figures 3.12 and 3.13 respectively. The temperatures of the representative slices have been chosen to illustrate the inelastic scattering at base temperature, $T \simeq 1/2\ T_g$, $T \simeq T_g$ and $T \geq 2\ T_g$. In contrast to $NaNiO_2$, there is no evidence of spin waves or other inelastic excitations, and the temperature dependence of the inelastic signal is far more subtle. On the basis of the representative datasets shown in figures 3.12 and

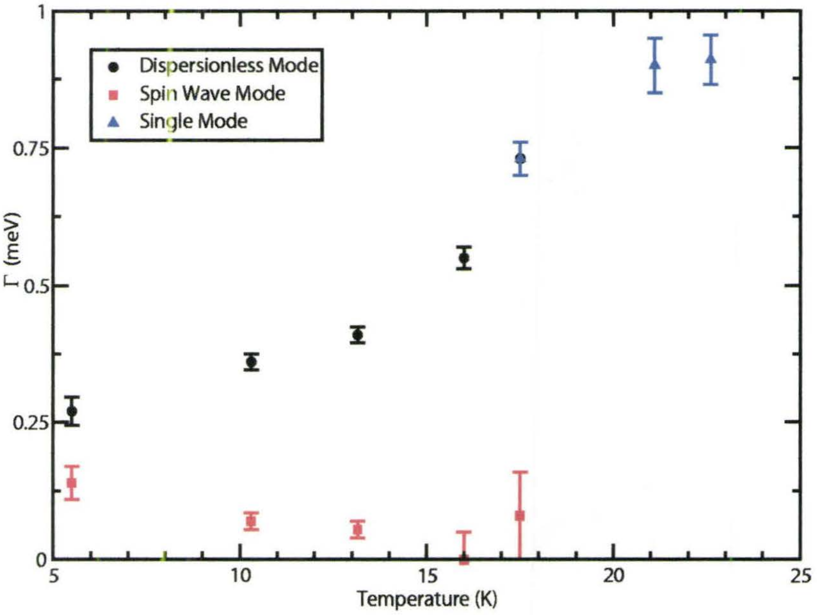

Figure 3.11: Inelastic peak width as a function of temperature for $NaNiO_2$.

3.13 there appear to be no qualitative differences between the inelastic scattering of samples (D) and (X). Furthermore, in both samples the temperature evolution of the inelastic signal appears to take place almost entirely below T_g, with datasets at T_g and $3 \times T_g$ being almost indistinguishable.

The most striking feature which emerges from the E vs $|Q|$ slices is the development of broad inelastic scattering in the low-$|Q|$ region. This scattering extends in $|Q|$ from approximately 0 to 0.6 $\AA^{-1}$, reaching a maximum energy of $\sim$ 0.8 meV. It may be particularly significant to note that the end of the low-$|Q|$ inelastic scattering at $|Q| \sim 0.6$ $\AA^{-1}$ occurs quite close to the (0,0,1/2) position at $|Q| \sim 0.65$ $\AA^{-1}$. This may suggest a natural comparison to the inelastic features of paramagnetic $NaNiO_2$, after the spin wave mode has collapsed and the dispersion envelope has been filled with inelastic intensity. The low-$|Q|$ inelastic signal in $LiNiO_2$ is very weak at base temperature, but steadily increases in intensity until the system reaches T_g. This re-

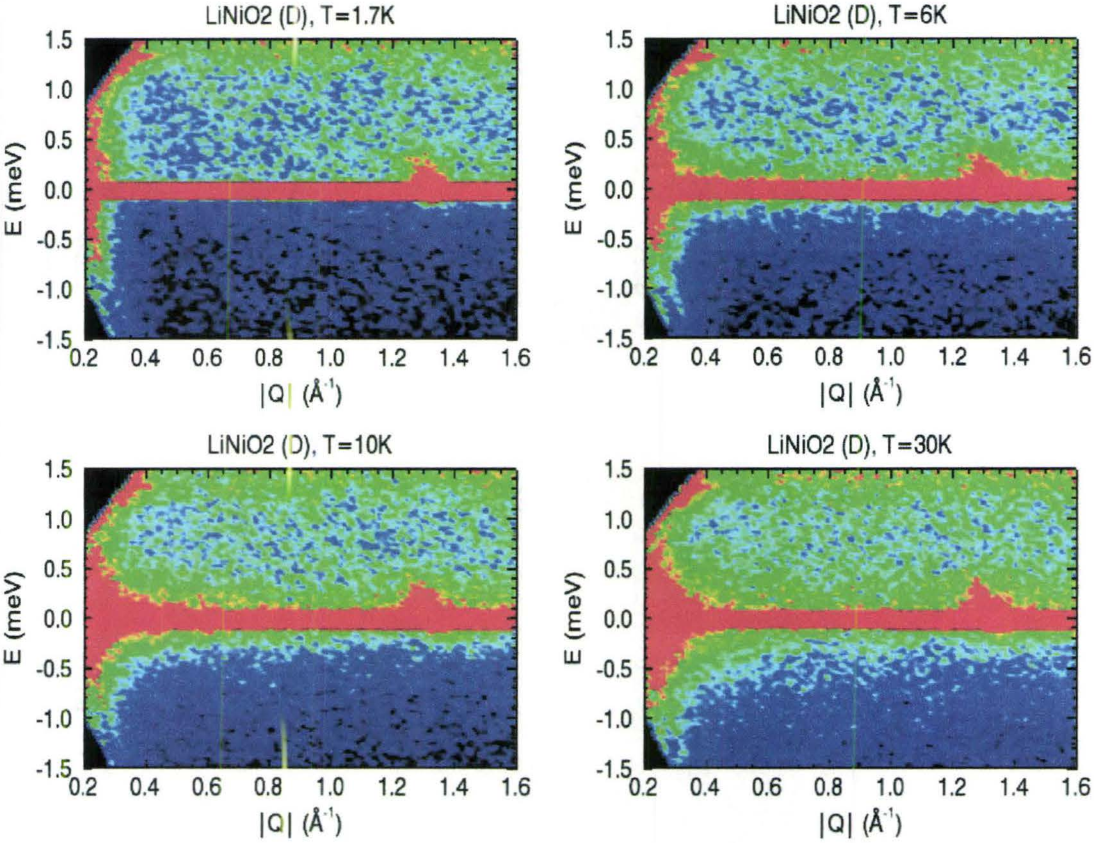

Figure 3.12: Representative data for $\mathrm{LiNiO_2}$ (D). Shown here are E vs. $|Q|$ slices collected at T = 1.7K, 6K, 10K ($\sim$ T_g), and 30K.

sult is exactly complementary to the measurements of the magnetic elastic scattering in section 4.2, which showed broad, low-$|Q|$ scattering that began to develop below T_g, and increased in intensity with decreasing temperature.

The temperature dependence of the inelastic scattering in $\mathrm{LiNiO_2}$ is perhaps more effectively illustrated in the form of colour contour maps, as shown in figures 3.14 and 3.15. Each of these maps is composed of a series of energy cuts, integrated over $0.5\ \mathring{A}^{-1} < |Q| < 0.8\ \mathring{A}^{-1}$, which have been collected over a range of temperatures from 1.7K to 30K. For display purposes, all of the scattering from the elastic channel has been omitted from the colour contour plots, and a correction has been applied to

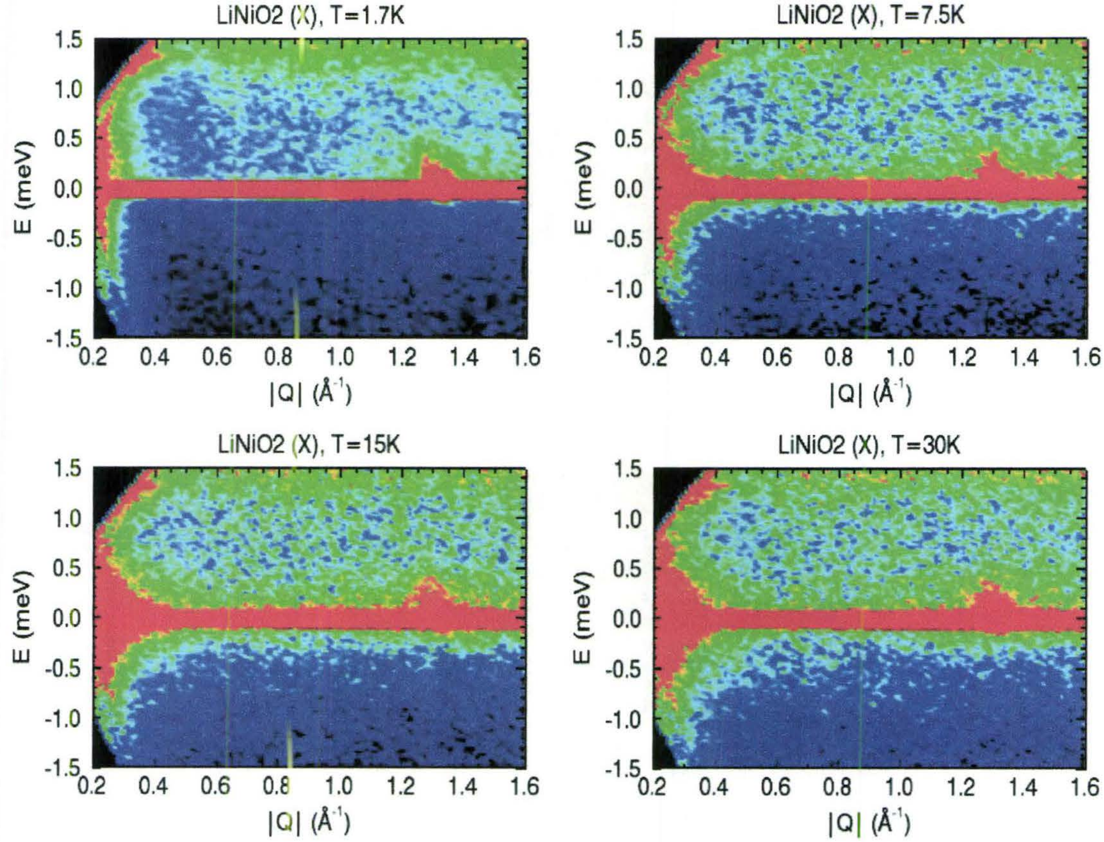

Figure 3.13: Representative data for $\mathrm{LiNiO_2}$ (X). Shown here are E vs. $|Q|$ slices collected at T = 1.7K, 7.5K, 15K ($\sim T_g$) and 30K.

remove the exponential background discussed in section 4.1.

At high temperatures, the spins of the system are free to fluctuate and behave dynamically. This is reflected in the measurements of the inelastic scattering, which reveal a broad energy spectrum and significant scattering intensity at large positive and negative energy transfers. As the temperature of the system gradually decreases, the width of the energy spectrum begins to narrow, and the weight of the inelastic intensity starts to shift towards smaller and smaller energy transfers. Spins fluctuations become slower, and some of the spins themselves become static. This process continues until the system reaches T_g, the glass transition, at which point almost all of the inelastic intensity collapses into the elastic channel. Below T_g, the inelastic spectrum remains extremely narrow and little inelastic intensity remains, even at very low energy transfers. This is the same spin freezing effect which was demonstrated by the plot of the integrated intensities shown earlier in figure 3.6.

A value of T_g can be estimated for each of the two samples based on the shape of the inelastic spectrum shown in figures 3.14 and 3.15. Using the point at which the strongest inelastic scattering appears to collapse fully into the elastic channel, the colour contour maps suggest that $T_g \sim$ 8K for $LiNiO_2$ (D) and $T_g \sim$ 7K for $LiNiO_2$ (X). Similar to our comparison of the integrated scattering intensities in section 4.2, these colour contour maps seem to show very little difference in the magnetic properties of $LiNiO_2$ (X) and (D). Once again, this stands in contrast to the results of our dc susceptibility measurements, which indicated a substantial gap between the transition temperatures of the two samples.

A more detailed analysis of the inelastic spectrum of $LiNiO_2$ was carried out by fitting a series of energy cuts from samples (X) and (D). These cuts were collected over the full set of measured temperatures, from 1.7K to 30K, and were integrated over a range of $|Q|$ from 0.5 to 0.8 $\AA^{-1}$. This choice of $|Q|$ was selected chiefly because

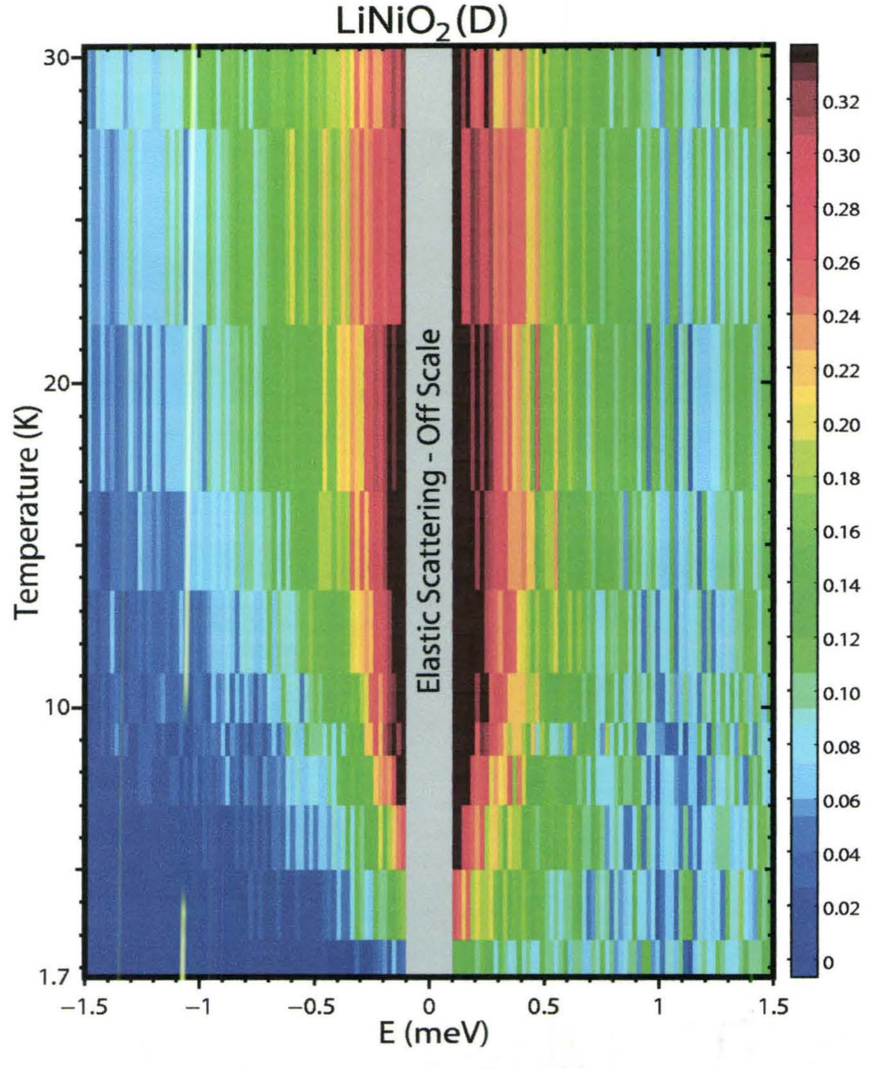

Figure 3.14: Colour contour map of the inelastic scattering in $LiNiO_2$ (D). The data has been corrected to account for the presence of exponential background scattering.

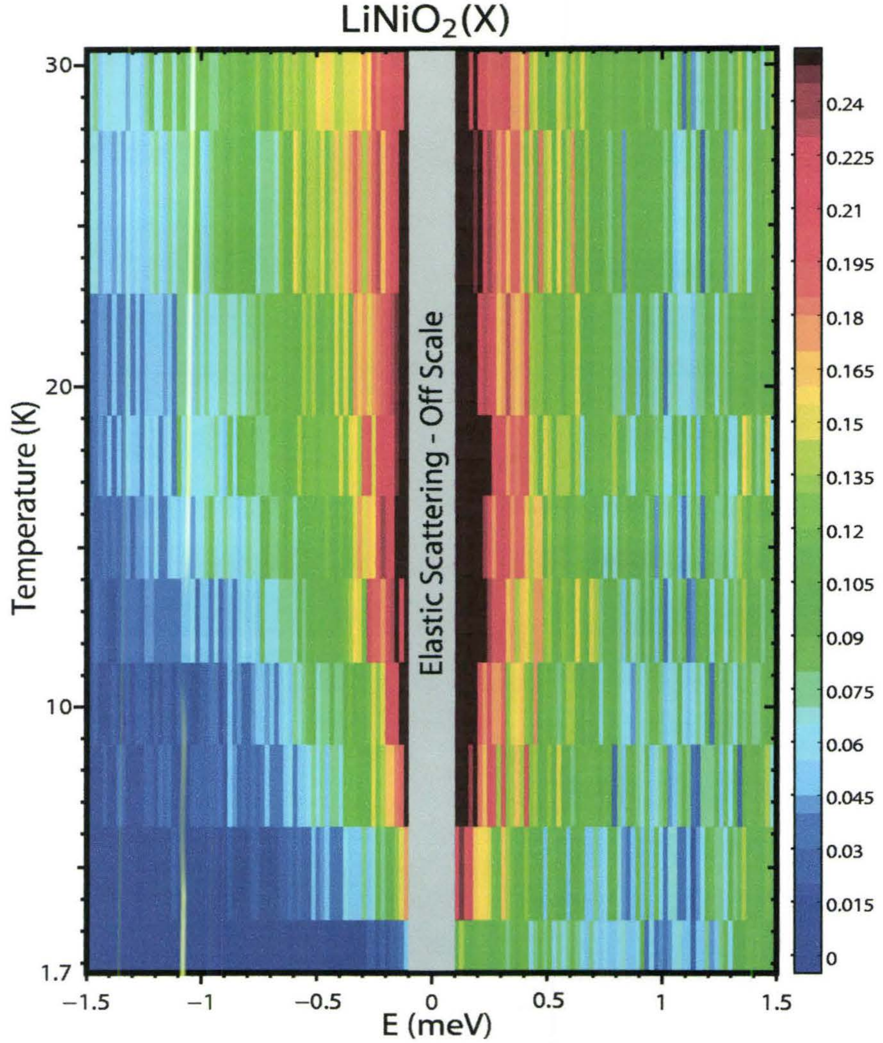

Figure 3.15: Colour contour map of the inelastic scattering in LiNiO$_2$ (X). The data has been corrected to account for the presence of exponential background scattering.

it surrounds the (0,0,1/2) position at $\sim 0.65\ \mathring{A}^{-1}$, the equivalent of the region in which both magnetic order and spin wave scattering were observed in $NaNiO_2$. A simple fit function of the form $I(E) = A \times N(E,T) \times \arctan\left(\frac{E}{\Gamma}\right)$ was chosen to describe the inelastic scattering intensity. As in the previous model for $NaNiO_2$, the parameters A and Γ refer to the amplitude and half-width of the fit function, while N(E,T) is the Bose thermal population factor. It should be noted this model was selected for purely phenomenological reasons. It is simply one of the simplest general forms which both satisfies detailed balance and appears to describe the shape of the inelastic spectrum. In the past, this model has also been successfully applied during the analysis of other spin glass systems, such as $Y_2Mo_2O_7$ [35]. An additional term was also added to the fit function to account for the presence of the exponential background described in section 4.1.

Several representative fits to the inelastic spectrum are shown in figure 3.16. The energy cuts provided in this figure were taken from $LiNiO_2$ (D), for the same choice of temperatures as the E vs. $|Q|$ slices shown in figure 3.12. As indicated by the quality of our fits, this choice of fit function provides a very reasonable description of the data. The most interesting information which can be extracted from our model is related to the behaviour of the width parameter, Γ, which describes the characteristic relaxation rate of the spins. The temperature dependence of Γ is described by the plot in figure 3.17.

Note that in both $LiNiO_2$ (X) and (D), the characteristic relaxation rate appears to decrease linearly as the temperature drops towards T_g. This is very similar to the behaviour of the relaxation rates observed in other spin glass materials such as $Y_2Mo_2O_7$ and SCGO [35]. The relaxation rate remains constant below T_g, with only very weak fluctuations occuring down to base temperature. Linear fits to the values of Γ above the glass transition suggest that the values of T_g are $\sim$ 9K and $\sim$ 5K for samples (D) and (X) respectively. While these results are reasonably consistent with the transition temperatures implied by the colour contour maps in figures 3.14 and 3.15, they only reiterate the previously observed discrepancy between the values of T_g observed through dc susceptibility and neutron scattering measurements. Although bulk dc susceptibility characterization implies that there are significant differences between $LiNiO_2$ (D) and (X), as far as the neutron time scale is concerned there appears to be little, if any, distinction between the two samples at all. As a final point of interest, comparisons of the temperature and fluctuation energy scales indicate that $k_B T_g \gg \Gamma$ over the whole of the measured temperature range. This would seem to indicate that the spin fluctuations in $LiNiO_2$ are classical, rather than quantum mechanical, in nature for $T < 3 \times T_g$.

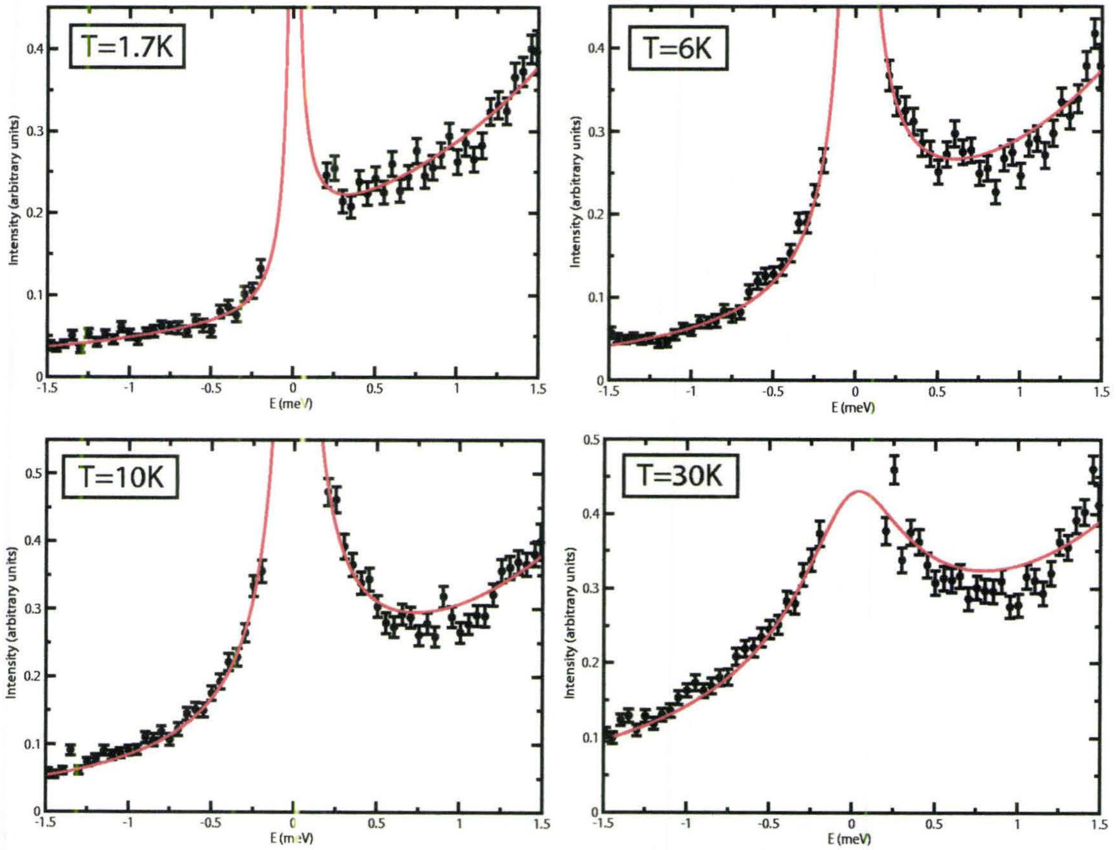

Figure 3.16: Representative fits of the inelastic spectrum in $LiNiO_2$. Energy cuts were performed for $0.5 \leq |Q| \leq 0.8$ $\mathring{A}^{-1}$.

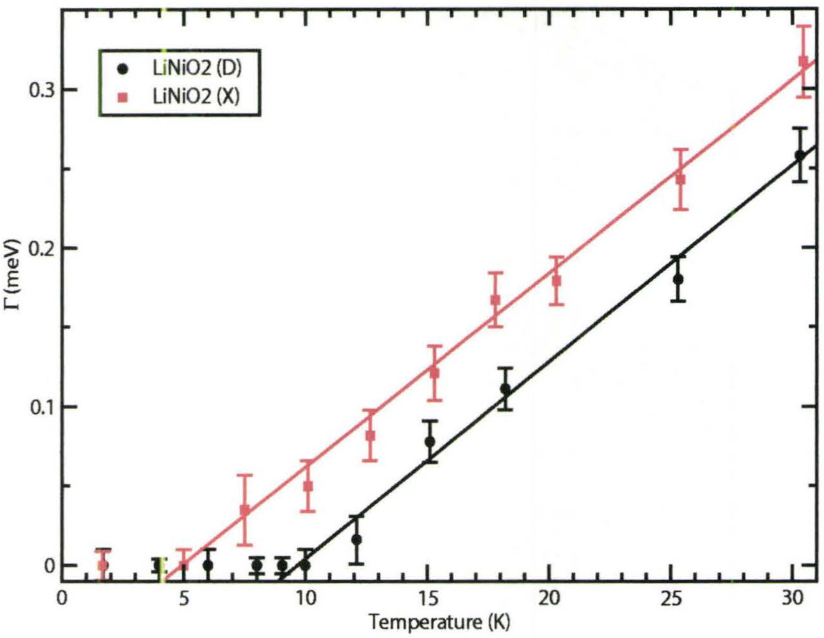

Figure 3.17: Inelastic peak width as a function of temperature for $LiNiO_2$.

Chapter 4

Conclusions

In the previous chapter, we demonstrated that a careful analysis of the neutron scattering measurements performed on $NaNiO_2$ and $LiNiO_2$ could yield a number of interesting experimental results. In $NaNiO_2$, our measurements revealed the trademarks of a magnetically ordered state below $T_N \sim 23K$. We observed the growth of magnetic Bragg peaks in the elastic channel, accompanied by the development of spin wave excitations in the inelastic channel. In $LiNiO_2$, we found no indication of long range magnetic or orbital order, but our measurements did provide evidence of a spin freezing transition in the vicinity of $T_g \sim 9K$. This behaviour, which is typical of a spin glass, was demonstrated by a significant narrowing of the inelastic energy spectrum and a collapse of inelastic scattering intensity into the elastic channel. In the final chapter of this thesis, I will attempt to draw a number of these results together, with the aim of explaining why the magnetic behaviour of $LiNiO_2$ and $NaNiO_2$ should be so different for two materials which appear to be so closely related in structure.

The key to understanding the origins of these two very different low temperature magnetic states may lie in the role of chemical disorder. While the crystal structures of $LiNiO_2$ and $NaNiO_2$ are identical at high temperatures, and are distinguished only by a small structural distortion even at low temperatures, the extent of the chemical disorder present in each of the two compounds is dramatically different. As noted in the introductory chapter, $NaNiO_2$ samples can be produced stoichiometrically and synthesized at very high purity. $LiNiO_2$ on the other hand, cannot be grown stoichiometrically and inherently contains disorder from the substitution of Ni^{3+} and Li^+ ions on neighbouring triangular planes. This form of ionic mixing is present at the level of $\sim 0.4\%$ even in the purest $LiNiO_2$ samples reported to date [13].

The potential effects of ionic mixing on the magnetic structures of $LiNiO_2$ and $NaNiO_2$ are illustrated in figure 4.1. Shown in panel A is the observed magnetic structure of $NaNiO_2$, and what one might presume to be the hypothetically ideal magnetic structure for $LiNiO_2$. The magnetically ordered state in A consists of triangular planes of ferromagnetically aligned spin 1/2 moments, which are stacked in an antiferromagnetic fashion along the *c*-axis. The system can be described in terms of two exchange couplings, J and J', which refer to the intra-plane ferromagnetic interaction and the inter-plane antiferromagnetic interaction respectively. If a magnetic impurity is added to the system, in the form of an additional Ni^{3+} ion substituted onto a Li^+ or Na^+ site, then a third exchange coupling, J", will be introduced. This is the situation depicted in panel B of figure 4.1. It is important to note that J" will result in frustration of the magnetic stacking sequence, regardless of whether it couples ferromagnetically or antiferromagnetically to the neighbouring spins. To make matters worse, this frustrating interaction is likely to be just as strong or stronger than J' since it will act over exactly half the distance between spins.

This argument appears to provide a natural explanation for the absence of magnetic ordering in $LiNiO_2$, which due to its intrinsic chemical disorder contains magnetic impurities on the order of 0.4% or more. Thus, ionic mixing between the

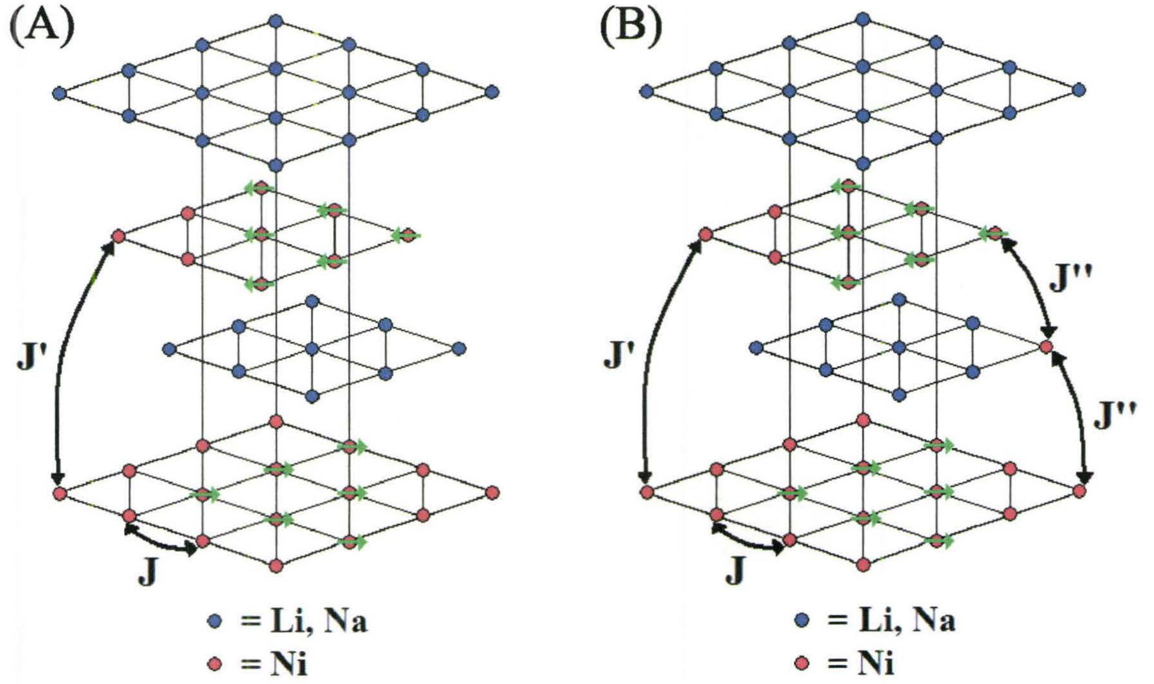

Figure 4.1: The effect of ionic mixing on the magnetic structure of $LiNiO_2$ and $NaNiO_2$. Shown in (A) is the ideal structure of $LiNiO_2$ and $NaNiO_2$ in the absense of ionic mixing. This is the observed magnetic structure in $NaNiO_2$ for $T < T_N$. Shown in (B) is the same structure, with a single Ni ion substituted onto one of the Li/Na sites. Note that the addition of Ni magnetic impurities in (B) will lead to the creation of a new exchange path, J", resulting in stacking sequence frustration.

Ni^{3+} and Li^+ sublattices can be expected to result in severe frustration of the inter-layer magnetic interactions. It is this magnetic frustration, in turn, which prevents the establishment of a magnetically long range ordered state at low temperatures.

One might expect from this conclusion that there should be clear similarities between the neutron scattering measurements performed on $LiNiO_2$ and paramagnetic $NaNiO_2$, and indeed this appears to be the case. A comparison of representative E vs. $|Q|$ slices from the two materials is provided in figure 4.2. $LiNiO_2$ (D) and

(X) are each shown for temperatures near their respective glass transitions, where the broad inelastic feature in the low-$|Q|$ region has become fully developed. The $NaNiO_2$ data is shown near the magnetic phase transition at T_N, where the spin wave mode has collapsed, and the remains of its dispersion envelope have been filled with inelastic intensity. Beyond the obvious qualitative resemblance between the two materials, there appears to be a very close relationship between the wide low-$|Q|$ features visible in each of the slices. Note that this broad inelastic scattering covers an almost identical range of energy and momentum transfers, extending from $|Q| = 0$ to $|Q| \sim 0.6$ or 0.65 $\AA^{-1}$, and reaching a peak of approximately 0.7 meV in E. Furthermore, there is an excellent match between the shapes of the inelastic energy spectra for each material. This can be demonstrated by the representative E cuts provided in the bottom panel of figure 4.2.

It is the comparison of the $|Q|$-ranges which may be particularly significant, since it indicates that in both $LiNiO_2$ and paramagnetic $NaNiO_2$ the majority of the inelastic scattering is bound between $|Q| = 0$ and the (0,0,1/2) position. Admittedly, this result is hardly surprising for $NaNiO_2$, since we already know that the low-$|Q|$ feature develops from the collapse of a spin wave mode which passes through the (0,0,1/2) magnetic zone center. However, it is a fact that carries far more important implications in the case of $LiNiO_2$, since it suggests that the inelastic scattering in the low-$|Q|$ region represents a collapsed spin wave, or perhaps more accurately, the precursor to a spin wave that might have developed in the absence of ionic mixing. This is one further piece of evidence which indicates that the difference between the observed low temperature states of $LiNiO_2$ and $NaNiO_2$ can be explained by the presence of magnetic frustration induced by chemical disorder.

There is still much about the magnetic behaviour of $LiNiO_2$ and $NaNiO_2$ which remains to be studied. However, in order for significant progress to occur, it is

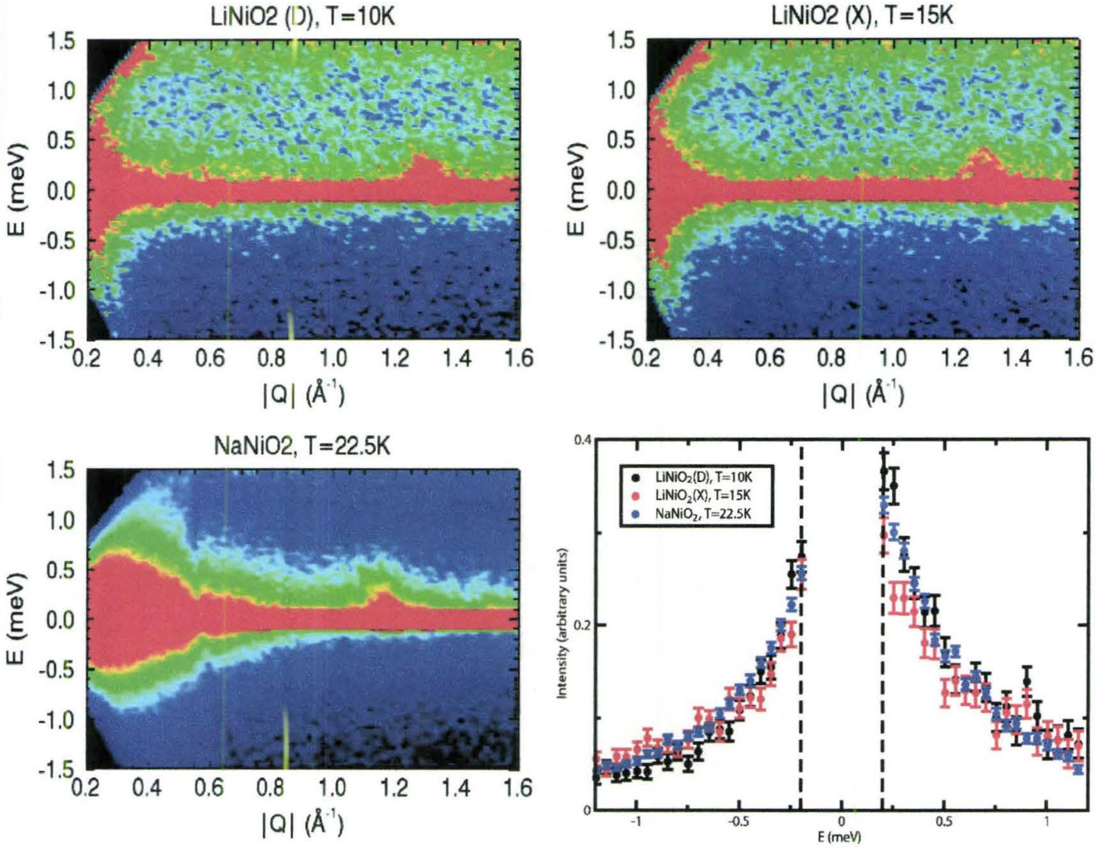

LiNiO2 (D), T=10K

LiNiO2 (X), T=15K

NaNiO2, T=22.5K

Figure 4.2: A comparison of neutron scattering measurements on $LiNiO_2$ and $NaNiO_2$. Shown here are representative E vs. $|Q|$ slices collected at T = 10K $\sim$ T_g for $LiNiO_2$ (D), T = 15K $\sim$ T_g for $LiNiO_2$ (X), and T = 22.5K $\sim$ T_N for $NaNiO_2$. Also provided is a comparison of E cuts taken through each data set, integrated over Q-ranges of $0.5 < |Q| < 0.8\AA^{-1}$ for $LiNiO_2$ and $0.49 < |Q| < 0.51\AA^{-1}$ for $NaNiO_2$.

almost essential to obtain high quality single crytals of these materials. While it is possible to gain a variety of useful information from measurements on polycrystalline and powder samples (as the last chapter has hopefully demonstrated), ultimately the information conveyed by such measurements can only describe the magnitude of the momentum transfer, $|Q|$, and reveals nothing about its direction in reciprocal space. Having the ability to probe specific directions in H, K, and L would be a huge advantage for future studies of $LiNiO_2$ and $NaNiO_2$, especially since both materials are already known to exhibit behaviour which is anisotropic and quasi-two-dimensional in nature.

While efforts to synthesize single crystal samples of $LiNiO_2$ and $NaNiO_2$ have proved unsuccessful in the past, it is heartening to note that considerable advances have recently been made towards single crystal growth of other stacked triangular ABO_2 compounds, such as $CuFeO_2$ [36]. The use of floating zone image furnace techniques, in particular, seems to offer a great deal of promise for future attempts at single crystal growth. In this respect, it is certainly fortunate that $LiNiO_2$ is a material with potentially profitable commercial applications, as it means that the system will likely continue to attract both scientific and industrial interest for many years to come.

Bibliography

[1] M. Lewis, B. Gaulin, L. Filion, C. Kallin, A. Berlinsky, H. Dabkowska, Y. Qiu, and J. Copley, Physical Review B **72**, 014408 (2005).

[2] K. Hirakawa, H. Kadowaki, and K. Ubukoshi, Journal of the Physical Society of Japan **54**, 3526 (1985).

[3] K. Hirakawa, R. Osborn, A. Taylor, and K. Takeda, Journal of the Physical Society of Japan **59**, 3081 (1990).

[4] Y. Li, M. Ma, D. Shi, and F. Zhang, Physical Review Letters **81**, 3527 (1998).

[5] F. Vernay, K. Penc, P. Fazekas, and F. Mila, Physical Review B **70**, 014428 (2004).

[6] J. Reimers, J. Dahn, J. Greedan, C. Stager, G. Liu, I. Davidson, and U. von Sacken, Journal of Solid State Chemistry **102**, 542 (1993).

[7] A. Bajpai and A. Banerjee, Physical Review B **55**, 12439 (1997).

[8] J. Kemp, P. Cox, and J. Hodby, Journal of Physics: Condensed Matter **2**, 6699 (1990).

[9] R. Stoyanova, E. Zhecheva, and C. Friebel, Journal of Physics and Chemistry of Solids **54**, 9 (1993).

[10] A. Rougier, C. Delmas, and G. Chouteau, Journal of Physics and Chemistry of Solids **57**, 1101 (1996).

[11] Y. Kitaoka, T. Kobayashi, A. Koda, H. Wakabayashi, Y. Niino, H. Yamakage, S. Taguchi, K. Amaya, K. Yamaura, M. Takano, A. Hirano, and R. Kanno, Journal of the Physical Society of Japan **67**, 3703 (1998).

[12] M. Nunez-Regueiro, E. Chappel, G. Chouteau, and C. Delmas, The European Physical Journal B **16**, 37 (2000).

[13] E. Chappel, M. Nunez-Regueiro, S. de Brion, and G. Chouteau, Physical Review B **66**, 132412 (2002).

[14] H. Yoshizawa, H. Mori, K. Hirota, and M. Ishikawa, Journal of the Physical Society of Japan **59**, 2631 (1990).

[15] K. Hirota, Y. Nakazawa, and M. Ishikawa, Journal of Physics: Condensed Matter **3**, 4721 (1991).

[16] P. Ganguly, V. Ramaswamy, I. Mulla, R. Shinde, P. Bakare, S. Ganapathy, P. Rajamohanan, and N. Prakash, Physical Review B **46**, 11595 (1992).

[17] D. Mertz, Y. Ksari, F. Celestini, J.-M. Debierre, A. Stepanov, and C. Delmas, Physical Review B **61**, 1240 (2000).

[18] F. Reynaud, D. Mertz, F. Celestini, J.-M. Debierre, A. Ghorayeb, P. Simon, A. Stepanov, J. Voiron, and C. Delmas, Physical Review Letters **86**, 3638 (2001).

[19] J. Greedan, Journal of Materials Chemistry **11**, 37 (2001).

[20] P. Anderson, Materials Research Bulletin **8**, 153 (1973).

[21] A. Rougier, C. Delmas, and A. Chadwick, Solid State Communications **94**, 123 (1995).

[22] E. Chappel, M. Nunez-Regueiro, G. Chouteau, O. Isnard, and C. Darie, The European Physical Journal B **17**, 615 (2000).

[23] J.-H. Chung, T. Proffen, S. Shamoto, A. Ghorayeb, L. Croguennec, W. Tian, B. Sales, R. Jin, D. Mandrus, and T. Egami, Physical Review B **71**, 064410 (2005).

[24] E. Chappel, M. Nunez-Regueiro, F. Dupont, G. Chouteau, C. Darie, and A. Sulpice, The European Physical Journal B **17**, 609 (2000).

[25] K. Yamaura, M. Takano, A. Hirano, and R. Kanno, Journal of Solid State Chemistry **127**, 109 (1996).

[26] P. Bongers and U. Enz, Solid State Communications **4**, 153 (1966).

[27] J. van Duijn, B. Gaulin, J. Park, S.-H. Lee, and J. Copley, preliminary study (unpublished).

[28] V. Sears, Neutron News **3**, 26 (1992).

[29] J. Copley and J. Cook, Chemical Physics **292**, 477 (2003).

[30] J. Copley, I. Peral, and Y. Qiu, *DCS User's Guide*, NIST Center for Neutron Research, last modified April 8, 2004, available online at: www.ncnr.nist.gov/instruments/dcs/dcs_usersguide/index.html.

[31] C. Windsor, *Pulsed Neutron Scattering* (Taylor and Francis, London, 1981).

[32] J. Ruff, private communication (unpublished).

[33] M. Plischke and B. Bergersen, *Equilibrium Statistical Physics*, 2nd ed. (World Scientific, Singapore, 1994).

[34] H. Kawamura, Journal of the Physical Society of Japan **58**, 584 (1989).

[35] J. Gardner, B. Gaulin, S.-H. Lee, C. Broholm, N. Raju, and J. Greedan, Physical Review Letters **83**, 211 (1999).

[36] O. Petrenko, G. Balakrishnan, M. Lees, D. Paul, and A. Hoser, Physical Review B **62**, 8983 (2000).